Developmental and tumour angiogenesis requires the mitochondria-shaping protein Opa1.

Stéphanie Herkenne[1,2], Olivier Ek[1], Margherita Zamberlan[1,2], Anna Pellattiero[2], Maya Chergova[1,2], Iñigo Chivite[3,4,5] Eliška Novotná[1,2], Giovanni Rigoni[1], Tiago Branco Fonseca[1,2], Dijana Samardzic[2], Andrielly Agnellini[6], Camilla Bean[1,2], Giulietta Di Benedetto[2,7], Natascia Tiso[1], Francesco Argenton[1], Antonella Viola[6], Maria Eugenia Soriano[1], Marta Giacomello[1], Elena Ziviani[1], Gabriele Sales[1], Marc Claret[3.4.5], Mariona Graupera[8,9], and Luca Scorrano[1,2*]

[1]Department of Biology, University of Padova, Via U. Bassi 58B, 35121 Padova, Italy
[2]Veneto Institute of Molecular Medicine, Via Orus 2, 35129 Padova, Italy
[3]Neuronal Control of Metabolism Laboratory, Institut d'Investigacions Biomèdiques August Pi i Sunyer (IDIBAPS), 08036 Barcelona, Spain
[4]CIBER de Diabetes y Enfermedades Metabólicas Asociadas (CIBERDEM), Barcelona, Spain
[5]School of Medicine, Universitat de Barcelona, Barcelona, Spain
[6]Department of Biomedical Sciences, University of Padova, Via U. Bassi 58B, 35121 Padova, Italy
[7]Institute of Neuroscience, CNR, Padova, Italy
[8]Vascular Signalling Laboratory, ProCURE and Oncobell Programs, Institut d'Investigació Biomèdica de Bellvitge (IDIBELL), Gran Via de l'Hospitalet 199, 08908 l'Hospitalet de Llobregat, Barcelona, Spain
[9]CIBERONC, Instituto de Salud Carlos III, Av. de Monforte de Lemos, 5, 28029, Madrid, Spain;

Characters count: 37,832

* Lead and Corresponding author. Luca Scorrano: luca.scorrano@unipd.it

Summary

While endothelial cell (EC) function is influenced by mitochondrial metabolism, the role of mitochondrial dynamics in angiogenesis, the formation of new blood vessels from existing vasculature, is unknown. Here we show that the inner mitochondrial membrane mitochondrial fusion protein Optic Atrophy 1 (OPA1) is required for angiogenesis. In response to angiogenic stimuli, OPA1 levels rapidly increase to limit nuclear factor kappa-light-chain-enhancer of activated B cells (NFκB) signaling, ultimately allowing angiogenic genes expression and angiogenesis. Endothelial Opa1 is indeed required in an NFκB-dependent pathway essential for developmental and tumor angiogenesis, impacting on tumor growth and metastatization. A first-in-class small molecule specific OPA1 inhibitor confirms that EC Opa1 can be pharmacologically targeted to curtail tumor growth. Our data identify Opa1 as a crucial component of physiological and tumor angiogenesis.

Keywords: mitochondria; Opa1; angiogenesis; tumor; metastasis

Introduction

Angiogenesis, the new blood vessel formation from preexisting vasculature, is crucial for embryogenesis, tissue healing, ovulation and placental vascularization (Carmeliet, 2005a). In response to pro-angiogenic stimuli, endothelial cells (ECs) specialize into different subtypes, each performing specific functions: tip cells, highly responsive to vascular endothelial growth factor (VEGF), extend filopodia at the forefront of the vascular branch and guide its migration but are poorly proliferative; stalk cells, in which VEGF receptor 2 (VEGFR2) signaling is suppressed, are located behind the tip cells and proliferate to extend the vascular branch (De Smet et al., 2009; Gerhardt et al., 2003; Potente et al., 2011). Once the vessel is formed and perfused, ECs become quiescent phalanx cells. Not surprisingly, such a complex specialization process is coordinated by a plethora of signaling factors including paracrine and autocrine factors, shear stress and even metabolic cues (Carmeliet, 2005b; Gerhardt et al., 2003; Phng and Gerhardt, 2009). Despite that angiogenesis is an energy-consuming process and that ECs have immediate access to blood oxygen, their metabolism is largely glycolytic (Cruys et al., 2016; Dobrina and Rossi, 1983; Krutzfeldt et al., 1990), impacting on angiogenesis *in vivo* (Dobrina and Rossi, 1983; Harjes et al., 2012; Harjes et al., 2016; Zecchin et al., 2017). A corollary of the glycolytic nature of ECs metabolism is that our knowledge on the role of mitochondria in angiogenesis is scant: angiogenic stimulation increases mitochondrial respiration (Guo et al., 2017) and mitochondria derived metabolites are essential to fuel cell proliferation and to keep signaling cascades in check. Indeed, PGC1α, the master regulator of mitochondrial biogenesis, is induced in ECs by several proangiogenic factor such as VEGF, hypoxia or caloric restriction. The

PGC1α-dependent mitochondrial biogenesis is a protective mechanism of ECs against oxidative stress (Afolayan et al., 2016; Patten and Arany, 2012; Valle et al., 2005). However, function of mitochondria extends far beyond their role in energy conversion as they participate in complex cellular processes: apoptosis, immune signaling, even differentiation (Pernas and Scorrano, 2016).

Mitochondrial function is dynamically controlled by mitochondrial shape and morphology, depending on the balance between fusion and fission processes (Pernas and Scorrano, 2016). Fission occurs upon the recruitment of dynamin-related protein 1 (DRP1) on the outer mitochondrial membrane (OMM), where it binds to its adaptors, fission 1 (Fis1), mitochondrial fission factor (MFF), and mitochondrial division (Mid) 49 and 51. Mitochondrial fusion is controlled by mitofusins (MFN) 1 and 2 in the OMM and by optic atrophy protein 1 (OPA1) in the inner mitochondrial membrane (IMM) (Chen et al., 2003; Cipolat et al., 2004). Independently from its role in mitochondrial fusion, OPA1 regulates apoptosis by participating in cristae junction formation and maintenance (Cipolat et al., 2006; Frezza et al., 2006). In addition, OPA1 stabilizes respiratory chain super-complexes, controlling mitochondrial respiratory activity and mitochondria-dependent cell proliferation (Cogliati et al., 2013). Because mitochondrial shape and dynamics can be modulated by cellular cues and are intimately linked to the functions of this organelle, cells can use them to regulate integrated cellular processes, like response to intracellular pathogens (Pernas et al., 2018) or cardiomyocyte differentiation, where mitochondrial fusion is required to properly tune gene expression (Kasahara et al., 2013).

To understand if mitochondria play a role in angiogenesis, we identify in publicly available datasets of gene profiling during angiogenesis transcriptional changes of key mitochondrial genes and in models of angiogenic stimulation EC mitochondrial elongation, associated with a rapid increase in Opa1 levels. By combining imaging, genetics, gene expression profiling as well as a small molecule first in kind Opa1 specific inhibitor, we show that Opa1 is required for angiogenesis and for tumor growth and metastatization, by impinging on NFκB activity and on angiogenic gene expression. Our data reveal a previously unappreciated role for Opa1 in the coordination of the angiogenic process.

Results

Angiogenic stimuli increase ECs Opa1 levels and mitochondrial length.

To investigate whether changes in mitochondrial shape are part of the angiogenic program, we took advantage of *kdrl:mCherry/kdrl-mls:GFP* transgenic *D. rerio* where blood vessel specifically express mitochondria -targeted GFP (mtGFP). Live imaging of these transgenic embryos showed elongated mitochondria in tip ECs (**Fig. 1A**). We recapitulated this finding *in vivo* in the mouse. We compared mitochondrial shape in different EC subtypes in the Endo-mitoGFP mouse that expresses mtGFP specifically in ECs (Pickles et al., 2013). Confocal imaging of live retinal mounts showed that mitochondria were fragmented in quiescent adult retinal phalanx ECs and in neonatal proliferating stalk ECs, tubular in the angiogenic active tip cells (**Fig. 1B-E**). Finally, mitochondria elongated also in a cellular model of angiogenesis, when Human Umbilical Vein Endothelial Cells (HUVEC) were exposed to different proangiogenic stimuli (VEGF, **Fig. 1F,G,** or bFGF and tumor conditioned medium, not shown).

To gain insight into the mechanism leading to mitochondrial elongation during angiogenesis, we resorted to the publicly available ANGIOGENES database of RNA sequencing during angiogenesis (http://angiogenes.uni-frankfurt.de). Even if replicated measurements for most genes in this dataset are lacking, we could operatively define differentially expressed genes (DEGs) by using an in-house generated statistical approximation method. We therefore computed and ranked the transcriptional changes of 20,185 human genes during VEGF treatment of HUVEC and we used this dataset to perform pathway analysis by SPIA (Tarca et al., 2009). By using Graphite, we collected human pathways from seven different databases (BioCarta, HumanCyc, KEGG,

PANTHER, PharmGKB, Reactome and SMPDB) and we ran the SPIA algorithm over all the resulting networks (Sales et al., 2012). Intriguingly, in addition to the expected pathways known to participate in angiogenesis, we retrieved several ones involving mitochondria (Supplementary Dataset 1). We therefore intersected the list of transcriptionally altered genes with the Human MitoCarta 2.0 database (https://www.broadinstitute.org/files/shared/metabolism/mitocarta/human.mitocarta2.0.html), identifying 994 mitochondrial genes whose transcription was dynamically modulated during VEGF stimulation of HUVEC. A heat map of Pearson-correlation clustered gene expression revealed that, among the fusion genes, only *OPA1* was upregulated early (**Fig**. **1H**). Back to the wet lab, we confirmed by real time PCR that in VEGF-stimulated HUVECs *OPA1* mRNA levels rapidly increased, whereas no changes in MFN1 and 2 expression were observed (**Fig. 1I**). Similarly, Opa1 protein levels increased ~3 fold 2h following VEGF treatment (**Fig. 1J**), suggesting that the observed mitochondrial elongation could be a consequence of the increased *OPA1* expression.

To understand if also *in vivo* Opa1 levels correlated with the elongated mitochondrial morphology observed in angiogenic active EC subtypes, we turned to the mouse retina model of physiological angiogenesis. Mouse retina is avascular at birth and blood vessels progressively sprout from the center towards the periphery until postnatal day 7 (P7). Simultaneously, blood vessels from the superficial (L1) vascular plexus start to sprout inside the retina to form the deeper plexus (L3). L1 contains stalk and tip cells from P2 to P6; at P8, L1 ECs become phalanx cells and L3 ECs are angiogenic (**Fig. 1K**) (Gerhardt et al., 2003; Stahl et al., 2010). In line with our *in vitro* data, we retrieved high OPA1 immunoreactivity in L1 tip cells at P4 (**Fig. 1L**). Conversely, at P11 the

angiogenic inactive L1 phalanx cells were barely immunoreactive for OPA1, as opposed to the strong OPA1 staining observed in the L3 angiogenic active ECs (**Fig. 1M**). Thus, Opa1 levels are higher and mitochondria are elongated in ECs undergoing angiogenic stimulation *in vitro* and *in vivo*.

Opa1 is required for angiogenesis *in vitro* and *in vivo.*

We next tested the physiological significance of the observed Opa1 levels increase triggered by angiogenic stimulation. First, we efficiently silenced *OPA1* by siRNA in HUVECs, obtaining the expected mitochondrial fragmentation (**Supplementary Fig. S1A-C**). While *OPA1*-silenced cells remained viable throughout the experiment (**Supplementary Fig. S1D**), all the measured angiogenic parameters: migration (**Supplementary Fig. S1E-F**), proliferation (**Supplementary Fig. S1G**) and tubulogenesis (**Supplementary Fig. S1H-I**) were curtailed. To determine whether these effects were specific for *OPA1* deletion or generically caused by the perturbation of mitochondrial fusion, we efficiently silenced MFN1 or MFN2 in HUVECs, causing again the expected mitochondrial fragmentation (**Supplementary Fig. S1J-L**). Nevertheless, while MFNs silencing induces a significant degree of ECs death (**Supplementary Fig. S1M**), all the angiogenic parameters of migration (**Supplementary Fig. S1N-O**), proliferation (**Supplementary Fig. S1P**) or tubulogenesis (**Supplementary Fig. S1Q-R**) were unaffected.

Comforted by these results, we decided to investigate if Opa1 influenced angiogenesis in vivo. First, we measured if angiogenesis was stimulated by increased Opa1 levels in the *Opa1^{tg}* mice (Varanita et al., 2015). OPA1 levels were slightly higher in *Opa1^{tg}*

primary mouse pulmonary endothelial cells (MPECs) that after two rounds of purification, the isolated MPECs expressed the EC markers VE-Cadherin, VEGFR2 and Endothelial specific molecule 1 (ESM1), confirming their endothelial identity (**Supplementary Fig. 2A,B**). Isolectin-B4 staining of retinal vessels of *Opa1*^{tg} P5 pups revealed a small but significant increase in the radial expansion of the retinal vascular plexus (**Fig. 2A-B**). Next, we decided to generate a mouse model of endothelial-specific *Opa1* ablation. *Opa1*$^{f/f}$ mice were crossed with Tg(Tek-cre) 2352Rwng mice expressing the Cre recombinase under the Tie2 promoter in ECs, generating EC Opa1 knockout animals (*Opa1*$^{\Delta EC/\Delta EC}$). *Opa1*$^{\Delta EC/\Delta EC}$ mice died during embryogenesis, but we could analyze heterozygous *Opa1*$^{\Delta EC/+}$ mice that were born in normal mendelian ratios and developed normally. We first evaluated the angiogenic parameters in primary MPECs from neonatal *Opa1*$^{+/\Delta EC}$ mice. As expected, Opa1 protein levels were reduced by 50% in purified *Opa1*$^{\Delta EC/+}$ MPECs (**Supplementary Fig. 2C**), and migration (**Fig. 2C-D**) as well as proliferation (**Fig. 2E**) were reduced, in line with what observed upon *OPA1* silencing in HUVEC. While these heterozygous *Opa1* MPEC were useful to confirm the specificity of the antiangiogenic effects observed upon *OPA1* silencing in HUVEC, we were still uncertain of whether angiogenesis *in vivo* required *Opa1*. Interestingly, isolectin-B4 staining of retinal vessels of *Opa1*$^{+/\Delta EC}$ pups at P4 revealed that ECs loss of OPA1 reduced radial expansion of the vascular plexus (**Fig. 2F-G**), diminished the number of vascular branch points (**Fig. 2H-I**), reduced the number of tip cells (**Fig. 2J-K**). In addition, Isolectin-B4 staining of retinal vessels of *Opa1*$^{+/\Delta EC}$ pups at P6 revealed that EC loss of OPA1 slightly reduced the venous branching (**Supplementary Fig. 2D-E**). Retinal veins can be theoretically assigned to three different regions: proximal (Vp,

located close to the optic nerve), central (Vc, in the middle of the plexus) and distal veins (Vd), responsible for the sprouting (**Supplementary Fig. 2F**). The slight venous branching reduction observed in *Opa1*$^{+/\Delta EC}$ pups was caused only by the decrease in Vd branching. Conversely, Vc and Vp branching were not affected (**Supplementary Fig. 2G**) like the arteriovenous patterning and the arterial branching (**Supplementary Fig. 2H-I**).

To investigate the effect of complete *Opa1* ablation *in vivo* and to avoid the potential issues of *Opa1* deletion in hematopoietic cells caused by the Tie2-Cre system (Kisanuki et al., 2001), we generated an inducible endothelial knockout model for *Opa1* (*Opa1*$^{i\Delta EC}$) by crossing *Opa1*$^{f/f}$ with Cdh5(PAC)-CreERT2 mice, expressing the Cre recombinase under the tamoxifen-inducible Vascular Endothelial (VE) cadherin promoter (Wang et al., 2010). Acute *Opa1* ablation was induced by a daily Tamoxifen injection from P1-P3, resulting in a significant *Opa1* mRNA reduction at P5 in MPECs from *Opa1*$^{i\Delta EC}$ pups (**Supplementary Fig. 2J**). Moreover, the efficiency of the tamoxifen induced *Opa1* deletion was also confirmed by OPA1 immunostaining in P6 retinal blood vessels (**Supplementary Fig. 2K**). Acute EC *Opa1* ablation curtailed radial vascular plexus expansion (**Fig. 2L-M**), vascular branch points (**Fig. 2N-O**), tip cells (**Fig. 2P-Q**), and slightly reduced venous branching (**Supplementary Fig. 2L-M**) because of the decrease in Vd branching, without any effect on Vc and Vp branching (**Supplementary Fig. 2N-O**) or arteriovenous patterning and arterial branching (**Supplementary Fig. 2P-Q**). These data indicate that Opa1 is essential for angiogenesis *in vivo*.

To explore the functional relevance of *in vivo* Opa1 ablation, we turned to *fli1a:EGFP* zebrafish embryos expressing GFP in ECs and analyzed only viable embryos without

major developmental alterations. Opa1-specific morpholino injected-embryos showed a reduction in Opa1 protein level 24 hours post-fertilization (hpf) (**Fig. 2R**), leading to mitochondrial fragmentation in intersomitic vessels (ISVs) (**Fig. 2S-T**). Functionally, the lack of Opa1 altered ISV sprouting, reducing the number and length of filopodia (**Fig. 2U-V**). To determine whether these effects were specific for *OPA1* deletion or generically caused by the perturbation of mitochondrial fusion, we generated an inducible endothelial knockout model for *Mfn1* (*Mfn1*$^{i\Delta EC}$) by crossing *Mfn1*$^{f/f}$ with *Pdgfb-iCreER* mice (Claxton et al., 2008). In line with the in vitro data, acute EC *Mfn1* ablation does not affect radial vascular plexus expansion (**Supplementary Fig 2R-S**), vascular branch points (**Supplementary Fig 2T-U**) or tip cells (**Supplementary Fig 2V-W**). Finally, the effect of EC Opa1 ablation was confirmed in a further mouse model of angiogenesis, the Matrigel plug assay. Vessel growth into Matrigel plugs (assayed by measuring hemoglobin content) was reduced in *Opa1*$^{+/\Delta EC}$ mice (**Fig. 2W-X**).

Our results indicated that in the absence of Opa1, angiogenesis was curtailed. However, they did not prove that Opa1 induction was required to modulate angiogenesis. To address this question, we first performed a small pharmacological screening to identify which pathway downstream of VEGF was responsible for Opa1 upregulation during angiogenesis. Inhibitors of ERK (PD98059), JAK/STAT (AG490) (Seo et al., 2009) and STAT3 (LLL12) (Lin et al., 2010) but not of PI3K/AKT pathways (wortmannin) curtailed *OPA1* upregulation and mitochondrial elongation downstream VEGF activation (**Fig. 3A and Supplementary Fig. 3A-C**). These data indicate that VEGF increases OPA1 levels via the MAPK and STAT3 pathways. Because inhibitors of these pathways interfere with multiple aspects of angiogenesis, they cannot be used

to directly test if Opa1 induction was required for angiogenesis. We therefore devised a genetic system where we could in principle specifically prevent the increase of *Opa1* downstream of VEGF. We generated *Opa1$^{f/f}$::Opa1^{tg}* mice by crossing *Opa1^{tg}* (Varanita et al., 2015) with *Opa1$^{f/f}$* mice (Cogliati et al., 2013). We isolated *Opa1$^{f/f}$::Opa1^{tg}* MPEC and we infected them with Cre adenoviruses to delete genomic, but not transgenic expression of Opa1 (**Supplementary Fig.3D**). As expected, *Opa1* mRNA expression levels were stable following Cre delivery in VEGF treated *Opa1$^{f/f}$::Opa1^{tg}* MPEC because the genomic locus responsible for it was excised (**Supplementary Fig.3E**). Cre-adenovirus infection of MPEC did not affect VEGF signaling per se, measured by following VEGF-induced ERK phosphorylation (**Fig. 3B**). Conversely, it curtailed OPA1 protein increase (**Fig. 3B**), mitochondrial elongation (**Supplementary Fig. 3F-G**), and strikingly the two key parameters of angiogenesis cell migration and proliferation (**Fig. 3C-D)**. Taken together, these results place the observed increase in Opa1 as a required component of angiogenesis *in vitro*, *ex vivo* and *in vivo*.

EC Opa1 is required for expression of angiogenic genes.

We next wished to understand the molecular mechanism by which Opa1 controls angiogenesis. Cell death could explain the observed antiangiogenic phenotype of Opa1 ablation, but because HUVECs Opa1 ablation did not induce it (**Supplementary Fig. 1D**), we investigated if the vascular defects were caused by an alteration of mitochondrial function. However, Opa1 ablation *in vitro* in HUVEC and *in vivo* in MPEC did not affect ATP levels (**Fig. 3E**), or HUVEC respiration and mitochondrial membrane potential (**Supplementary Fig. 3H,I**), leaving the mechanism by which Opa1 controls

angiogenesis unexplained. We therefore performed unbiased deep sequencing to investigate if gene expression was rewired by *Opa1* deletion. The comparison of RNA sequencing (RNAseq) data obtained from triplicate analyses of control and Opa1-ablated HUVECs indicated that 1226 genes out of a total of 16427 genes with measured expression were differentially expressed [fold change (FC) threshold=0.6; FDR=0.05; **Fig. 3F; extended dataset 2;** GEO: accession #GSE122042]. Interestingly, among the downregulated genes we retrieved, as expected, *OPA1* (FC=-1.32; FDR=$2.39x10^{-39}$), but also a number of genes involved in the promotion of angiogenesis like *SERPIND1* (FC=-1.52; FDR=$1x10^{-19}$); *SERPINH1* (FC=-0.77; FDR=$9x10^{-4}$); ID1 (FC=-0.9; FDR=0.005); PDGFC (FC=-0.64; FDR=$3x10^{-6}$) (Ikeda et al., 2012; Li et al., 2005; Qiu et al., 2011; Wu et al., 2016). Conversely, among the upregulated genes we found inhibitors of angiogenesis like Flt1, that interferes with the VEGF pathway (Ambati et al., 2006; Roberts et al., 2004) (**Fig. 3F**). We therefore tested by quantitative PCR (qPCR) the response of a panel of genes involved in angiogenesis to *OPA1* silencing in HUVEC. Remarkably, all pro-angiogenic genes tested were reduced, except for *EPHb4*, the venous markers involved in the arteriovenous patterning (Adams, 2003; Wilkinson, 2001), whereas FLT1 levels were increased (**Fig. 3G**). Thus, OPA1 silencing skews gene expression in HUVEC towards an anti-angiogenic state.

To get further insights into how an inner mitochondrial membrane protein can regulate gene expression, we used Ipathway^{TM} (Advaita) analysis to represent enriched signaling pathways that might account for the observed changes in gene expression profile upon *OPA1* silencing. Interestingly, a handful of apparently unrelated pathways were over-represented (**Fig. 3H**); at a closer look, these pathways shared a common trait

represented by the activation of NFκB. Indeed, reads for mRNAs of NFκB activators and target genes increased, while those for NFκB inhibitors were decreased in *OPA1*-ablated HUVECs (**Fig. 3I**). We therefore measured if these transcriptional changes were mirrored by differences in NFκB activity. NFκB catalytic P65 subunit activity was increased in *OPA1*-ablated ECs, as judged by a specific NFκB ELISA (**Fig. 3J**). Comforted by the fact that OPA1 but not the other fusion genes *MFN1* or *MFN2*, controlled NFκB in ECs (**Fig. 3J**), we verified if *OPA1* silencing interfered with the normal changes in NFκB activity during angiogenic stimulation. While NFκB activity declined rapidly after VEGF treatment in control HUVEC, this decrease was absent in *OPA1*-ablated HUVECs (**Fig. 3K**).

Opa1 regulates NFκB and angiogenesis by impinging on Ca^{2+} signaling.

NFκB is tightly controlled by its endogenous inhibitor IκBα whose degradation by the ubiquitin-proteasome system allows NFκB nuclear translocation and transcriptional activity (Kanarek et al., 2010). Interestingly, *OPA1* silencing led to IκBα degradation, as shown by specific immunoblotting (**Fig. 3L**). We next wished to ascertain which upstream pathway [AKT/mTOR/Raptor, Ca^{2+} signaling, ERK (Dan et al., 2008; Jiang et al., 2004; Lilienbaum and Israel, 2003)] connected *OPA1* silencing to IκBα degradation. Because in *OPA1*-deficient HUVEC ERK and AKT phosphorylation, as well as mTOR targets were unaffected (**Supplementary Fig. 3J and not shown**), we turned our attention to Ca^{2+} signaling that can be modulated by Opa1 (Fulop et al., 2011). Interestingly, Opa1 is retrieved among the interactors of MICU1 (Tomar et al., 2019), a

crucial regulator of the mitochondrial Ca^{2+} uniporter (MCU) that mediates Ca^{2+} uptake in mitochondria (Csordas et al., 2013).

We first addressed whether deletion of Opa1 impacted on MICU1-containing complexes. Blue Native gel electrophoresis (BNGE) indicated that upon acute deletion of Opa1 in MEFs, total MICU1 levels where unaffected, but levels of a ~720 KDa MICU1-MCU-Opa1-containing complex were decreased (**Fig 3M**). Functionally, this remodeling of the MCU complex organization upon Opa1 deletion was mirrored by changes in cytosolic Ca^{2+} levels, which were increased upon *Opa1*, and as expected upon *Micu1* ablation in HUVECs. Simultaneous *Opa1* and *Micu1* silencing did not lead to a further increase in cytosolic Ca^{2+}, confirming that Opa1 and Micu1 not only interact, but also lie in the same pathway modulating Ca^{2+} levels (**Fig. 3N**). Several experiments also indicated that *MICU1* and *OPA1* are placed in the same pathway controlling NFkB activity and angiogenesis. First, like Opa1, also MICU1 silencing in HUVECs reduced I□Bα levels (**Supplementary Fig. 3K**). Second, MICU1 silencing inhibited HUVEC migration, tubulogenesis and proliferation (**Supplementary Fig. 3L-Q**). Third, we did not measure any additive effects of the simultaneous *OPA1* and *MICU1* ablation on IκBα decrease (**Supplementary Fig. 3K**) or angiogenesis (**Supplementary Fig. 3L-Q**). Altogether, these data support a role for the Opa1-MICU1 axis in the regulation of Ca^{2+} levels and NFκB activity. We therefore wished to understand if the defects in angiogenesis caused by Opa1 ablation were Ca^{2+}-dependent. In Opa1-silenced HUVECs, the cell-permeant chelator BAPTA-AM (Tsien, 1980) could stabilize IκBα (**Fig. 3O**), and curtail the NFκB hyperactivation (**Fig. 3P**) as well as the defective migration (**Fig. 3Q-R**). *In vivo*, intraocular injection of BAPTA-AM corrected all the retinal vascular

defects (radial expansion, branch points, total venous branching and distal branching points) recorded in *Opa1*$^{+/\Delta EC}$ pups (**Fig. 3S-U**). Thus, Opa1 modulates angiogenesis by regulating cytosolic Ca^{2+} levels.

Opa1 regulates angiogenesis via NFκB.

To investigate whether the observed NFκB hyperactivation caused the antiangiogenic effect of Opa1 ablation, we first pharmacologically blocked NFκB. The well-characterized IκBα kinase inhibitor BAY11-7082 (Pierce et al., 1997) did not reduce basal HUVEC NFκB activity, but it normalized NFκB activation and HUVEC migration recorded upon *OPA1* silencing (**Supplementary Fig. 4A-B**). Comforted by these results, we decided to downregulate by siRNA the *P65* subunit of NFκB (**Supplementary Fig. 4C**). Similar to what observed upon pharmacological inhibition, *P65* siRNA normalized migration and tubulogenesis in HUVEC where OPA1 was simultaneously silenced (**Fig. 4A-E**). To further verify whether NFκB was required for the vascular defects caused by *Opa1* ablation, we generated a mouse model of endothelial-specific *Opa1* and *P65* ablation. The *Opa1*$^{+/\Delta EC}$ mice were crossed with *P65*$^{f/f}$ (Algul et al., 2007) to generate *P65,Opa1*$^{+/\Delta EC}$ mice (**Supplementary Fig. 4D-F**). As expected, Opa1 and p65 protein levels were reduced in MPECs isolated from the double mutant mouse (**Supplementary Fig. 4G**). Notably, all retinal vascular defects (radial expansion, branch points, total venous branching and distal branching points) recorded in *Opa1*$^{+/\Delta EC}$ mice were rescued in *P65,Opa1*$^{+/\Delta EC}$ mice (**Fig. 4F-J**). Consistent with the *in vitro* and mouse data, BAY11-7082 inhibited NFκB activation caused by *opa1* ablation also in zebrafish (without affecting the basal NFκB activity, **Supplementary**

Fig. 4H) and restored the ISVs sprouting defects observed in *opa1*-morphant embryos (**Fig. 4K-M**). Finally, we also confirmed that OPA1 and MICU1 acts on angiogenesis through the same NFκB pathway. In line with the observed NFκB activation upon *MICU1* ablation, when we simultaneously ablated *P65* we corrected the migration, tubulogenesis and proliferation defects caused by *MICU1* ablation (**Fig. 4N-S**). These results indicate that NFκB is required to mediate the anti-angiogenic effects of *OPA1* downregulation in all systems tested.

Endothelial *Opa1* ablation or pharmacological inhibition impairs tumor growth.

Because tumor growth requires angiogenesis, we analyzed if endothelial *Opa1* ablation had any effect on the size of several orthotopic tumor models. Growth of subcutaneously implanted mouse B16F10 melanoma as well as of mouse breast adenocarcinoma E0771 cells was curtailed in $Opa1^{+/\Delta EC}$ mice (**Fig. 5A-B**; **Supplementary Fig. 5A-B**). When we visualized tumor vessels by immunostaining melanomas for the endothelial marker CD31, we noticed the expected enlargement of vessels in tumors growing in control mice. Diameter of tumor vessels and vascularized tumor area were conversely decreased when melanomas were grown in $Opa1^{+/\Delta EC}$ mice, without affecting the total number of vessels (**Fig. 5C-E; supplementary Fig. 5C**). The observed reduction in tumor growth could be also caused by increased anti-tumor immunity in $Opa1^{+/\Delta EC}$ mice, where the Tie2 driver used to ablate Opa1 from ECs can also drive Cre expression (and hence Opa1 deletion) in myeloid cells. However, tumoral recruitment of myeloid cells (CD^{11+}, granulocytes, immature macrophages, macrophages and monocytes) was not affected in $Opa1^{+/\Delta EC}$ mice (**Supplementary**

Fig. 5D). We conclusively excluded this possibility by verifying if also acute *Opa1* EC ablation reduced tumor growth. To this end, *Opa1*$^{i\Delta EC}$ mice received a daily tamoxifen injection from P25-P30, resulting in a significant reduction in Opa1 mRNA in MPECs isolated from P60 *Opa1*$^{i\Delta EC/+}$ *and Opa1*$^{i\Delta EC}$ mice (**Supplementary Fig. 5E**). This acute endothelial Opa1 ablation curtailed growth of B16F10 melanomas subcutaneously implanted in 2-month old mice (**Fig. 5F-G**) and reduced the diameter of blood vessels and the vascularized area of the tumor, without affecting the total number of vessels (**Fig. 5H-J; Supplementary Fig.5F**). We also determined whether this effect was specific for Opa1 ablation or caused by a general perturbation of mitochondrial fusion. To this end, *Mfn1*$^{i\Delta EC}$ mice received a daily tamoxifen injection from P25-P30, resulting in a significant reduction in Mfn1 mRNA in MPECs isolated from P60 *Mfn1*$^{i\Delta EC}$ mice (**Supplementary Fig. 5G**). However, growth of subcutaneously implanted B16F10 melanomas was not affected in 2-month old *Mfn1*$^{i\Delta EC}$ mice (**Supplementary Fig. 5H-I**). Finally, we reasoned that tumor growth should be unaffected in *P65*,*Opa1*$^{+/\Delta EC}$ mice where angiogenesis occurs normally. Indeed, the subcutaneously implanted melanomas grew as efficiently in control and in *P65*,*Opa1*$^{+/\Delta EC}$ mice (**Figure 5K-L**). In addition, the reduction in blood vessels diameter and vascularized area observed in tumors grown in *Opa1*$^{+/\Delta EC}$ *and Opa1*$^{i\Delta EC}$ mice was not recorded when the same type of tumors were implanted in *P65*,*Opa1*$^{+/\Delta EC}$ mice (**Supplementary Fig. 5J-M**), further confirming that the effect of *Opa1* ablation was a direct consequence of impaired angiogenesis. In conclusion, endothelial Opa1 ablation impairs tumor growth by a specific effect on tumor vascularization.

These data indicated the interesting possibility that acute Opa1 inhibition in endothelial cells can counteract tumor growth and metastasis. We therefore setup a proof of principle experiment to verify whether acute pharmacological Opa1 inhibition could curtail tumor growth. Melanomas were subcutaneously implanted and after 10 days we delivered by peritumoral injection 10 mg/kg/die of N-(1,5-dimethyl-3-oxo-2-phenyl-2,3-dihydro-1H-pyrazol-4-YL)-3-methyl-1-PH+ (MYLS22), the first in class safe and specific Opa1 inhibitor discovered in our laboratory (Pellattiero et al., 2019) (**Supplementary Fig. 5N**). Remarkably, tumor growth was curtailed to the same extent observed in *Opa1*$^{+/\Delta EC}$ mice. Moreover, MYLS22 did not display any additive effect in *Opa1*$^{+/\Delta EC}$ mice, further confirming its specific Opa1 targeting (**Fig. 5M,N**). In conclusion, genetic as well as pharmacological inhibition indicate that Opa1 is a targetable component of tumor angiogenesis.

Endothelial Opa1 ablation prevents metastasis dissemination.

Angiogenesis is not only involved in tumor growth, but also in tumor dissemination. Comforted by the finding that EC Opa1 is required for tumor growth, we decided to investigate if also metastatization required EC Opa1. To this end, first we used the well-established experimental hematogenous metastasis assay in which B16F10 melanoma cells are injected in the tail vein (Elkin and Vlodavsky, 2001). Interestingly, the number of lung metastases was reduced by 75% in *Opa1*$^{+/\Delta EC}$ mice (**Fig. 6A,B**). Because in this model tumor cells were directly injected into circulation, the first steps of metastatic dissemination (extracellular matrix degradation, tumor cells migration and intravasation) cannot be investigated. We therefore turned to the B16F10 footpad melanoma model,

metastases of which depend on both angiogenesis and lymphangiogenesis (Agrawal et al., 2014). Primary tumor growth was reduced in monoallelic and inducible endothelial *Opa1* knockout mice (**Fig. 6C-D, F-G**). Because the foot lymphatic system drains through the popliteal lymph node (LN), primary B16F10 footpad tumors disseminate metastases to this popliteal LN. Interestingly, the frequency of sentinel LN metastases dropped from 48.5% in $Opa1^{f/+}$ (n=33 LN analyzed) to 20.8% in $Opa1^{+/\Delta EC}$ (n=24) and from 56.7% in $Opa1^{f/f}$ (n=30) to 28.6% in $Opa1^{i\Delta EC}$ (n=18). Even when metastases were identified in mice where EC Opa1 was deleted, their size was much smaller than that observed in their control littermates (**Fig. 6E,H**). In addition, cells were found in the lumen of blood vessels of primary melanomas implanted in the footpad of $Opa1^{f/f}$ but not $Opa1^{i\Delta EC}$ mice (**Fig. 6I**). Because EC *Opa1* deletion did not affect the number (and type) of tumor infiltrating immune cells (**Supplementary Fig. 5D**), these are likely intravasating tumor cells, further supporting that inducible Opa1 ablation in EC curtails hematogenous metastasis.

Tumor blood vessels are known to be enlarged and leaky because they are poorly covered by smooth muscle actin^{+} (SMA) pericytes, allowing intravasation of tumor cells to the circulation. We investigated whether the reduction of metastases dissemination in $Opa1^{+/\Delta EC}$ mice could be explained by the normalization of tumor vessels diameter and pericytes coverage (Nagy et al., 2009; Ribeiro and Okamoto, 2015). In EC ablated *Opa1* mice, tumor vessels were indeed smaller, less dense and more covered by pericytes (**Fig.6J-N**). While these results were reassuring, we could not exclude that the LN metastases reduction measured in the two models of EC *Opa1* ablation was a mere consequence of the observed reduction in primary tumor size. We therefore turned to

ear implanted B16F10 tumors, which are drained by the lymphatic system (Bobek et al., 2010). Primary tumor growth was unaffected in *Opa1*$^{+/\Delta EC}$ mice (**Fig. 6O,P**), but the frequency of sentinel LN metastases was curtailed from 90.9% in *Opa1*$^{f/+}$ (n=33) to 28.6% in *Opa1*$^{+/\Delta EC}$ mice (n=24). Moreover, size of the few metastases retrieved in *Opa1*$^{+/\Delta EC}$ LN was greatly reduced (**Fig. 6Q**).

Because tumor cells intravasation is orchestrated by pericyte-devoid lymphatic vessels (Cueni and Detmar, 2008), we reasoned that *Opa1* deletion might have affected also lymphatic vessels that differentiate from veins (Simons and Eichmann, 2013). Indeed, the drainage of ear-injected Evan's Blue that requires lymphangiogenesis was impaired in *Opa1*$^{+/\Delta EC}$ mice (**Supplementary Fig. 6A,B**). In addition, lymphatic vessels formation was affected by *opa1* ablation in live transgenic *stab1:YFP* zebrafish embryos, expressing YFP in the lymphatic system (**Supplementary Fig. 6C**). To discriminate whether *OPA1* ablation directly affected lymphatic function, or whether the lymphatic effects were secondary to venous defects, we turned to the lymphatic HMVEC-dly cellular model. *OPA1* silencing blunted HMVEC-dly migration (**Supplementary Fig. 6D,E**) and tubulogenesis (**Supplementary Fig. 6F-H**) without altering their proliferation (**Supplementary Fig. 6I**). Like in HUVECs, lymphatic *OPA1* ablation causes a rewiring of lymphatic genes expression: the key regulators of lymphatic function *PDPN*, *LYVE1*, *PROX1*, *FLT4* and *NRP2* (Kong et al., 2017; Ou et al., 2015) were downregulated upon *OPA1* ablation in HMVEC-dly (**Supplementary Fig. 6J**). In conclusion, EC Opa1 ablation curtails tumor metastatization by normalizing tumor vessels and reducing tumor lymphangiogenesis.

Discussion

The established notion that EC display a mostly glycolytic metabolism (Cruys et al., 2016; Dobrina and Rossi, 1983; Krutzfeldt et al., 1990) reduced the interest on the role of mitochondria in angiogenesis, until the recent discovery that fatty acid and amino acid oxidation pathways are essential for angiogenic sprouting (Potente and Carmeliet, 2017). However, whether mitochondria are involved in angiogenesis beyond their metabolic role is unknown. Our results indicate that the key fusion and cristae biogenesis protein Opa1 is recruited by the angiogenesis signaling cascade to provide the appropriate cues orchestrating vessel neoformation.

A handful of studies suggest that under pathological conditions mitochondrial dynamics can modulate ECs functions. For example, hyperglycemia induces DRP1-dependent ROS production in ECs (Makino et al., 2010; Paltauf-Doburzynska et al., 2004; Shenouda et al., 2011). However, the key question of whether and to which extent mitochondrial dynamics participates in developmental angiogenesis remained unanswered. The involvement of mitochondria and mitochondrial dynamics in angiogenesis does not seem so surprising, given the energy demanding nature of this process. However, ECs mostly depend on glycolysis for ATP biosynthesis, raising the question of whether mitochondria participate at all in physiological angiogenesis. Our results not only identify a key mitochondrial protein as an essential component of angiogenesis, but they also extend the role of mitochondria in ECs beyond energy conversion. Mitochondrial elongation in response to angiogenic stimuli *in vitro* or *in vivo* in the developing mouse retinal and zebrafish intersomitic vessels is prominent and associated with an early increase in Opa1 levels. By capitalizing on several purposely

generated *in vitro* and *in vivo* models of constitutive and inducible Opa1 ablation in ECs, we unveil that Opa1 is essential for ECs migration, branching and filopodia number and length in tip cells. These processes require the integration of multiple signals to produce the appropriate space- and time-ordered cellular responses. It is noticeable that the role of OPA1 in angiogenesis does not depend on its established function in apoptosis and mitochondrial respiration (Cogliati et al., 2013; Frezza et al., 2006). Our data also exclude the possibility that mitochondrial fusion per se controls angiogenesis: the outer membrane MFNs are not regulated by angiogenic cues and dispensable for developmental and tumor angiogenesis, even if *MFN1* or *MFN2* ablation causes ECs apoptosis (Lugus et al., 2011). We therefore posit that the effect of OPA1 is specific and mediated by its ability to control transcription of essential angiogenes. Indeed, unbiased gene expression analysis reveals changes in the levels of 7.5% of the measured transcripts upon *OPA1* deletion, among which a handful of essential angiogenic genes. Since our discovery that mitochondrial fusion directs cardiomyocyte differentiation and heart development by controlling transcription (Kasahara et al., 2013), mitochondrial morphology has been shown to control hematopoietic (Luchsinger et al., 2016) and mesenchymal stem cells (Forni et al., 2016) differentiation. It is interesting to note that fusion is embedded in these differentiation programs because of its ability to modulate transcription. Angiogenesis is no exception to this paradigm: Opa1 is placed at the crossroad between mitochondrial Ca^{2+} uptake and NFκB signaling to allow angiogenesis. When Opa1 is lacking, constitutive NFκB activation skews gene expression against angiogenesis, as demonstrated by genetic and pharmacological models of NFκB inhibition.

NFκB is a master regulator of EC function. While a handful of studies describe endothelial NFκB activation as proangiogenic (Andras et al., 2005; Kaplan et al., 2005; Soler et al., 1999), several reports illustrate the antiangiogenic effect of NFκB activation (Castellino and Ploplis, 2005; Mountain et al., 2007; Popov and Simionescu, 2006; Wilczynska et al., 2006; Xiao et al., 2005). Moreover, different types of angiogenesis inhibitors work through NFκB activation (Chen et al., 2006; Gingras et al., 2003; Tabruyn et al., 2003; Tadros et al., 2003), and transgenic mice expressing a dominant negative IκBα mutant under the control of Tie-2 promoter show an increase in tumor growth, further supporting an inhibitory role for NFκB in tumor angiogenesis (Kisseleva et al., 2006).

Because OPA1 can regulate vascular biology, we explored its role in tumor growth and metastatization. Endothelial *Opa1* is critical for tumor growth and for metastasis dissemination via lymphangiogenesis, providing a genetic proof of principle for targeted OPA1 inhibitors to treat angiogenesis-related diseases and cancer. This paradigm is further confirmed by the remarkable inhibition of tumor growth observed upon treatment with MYLS22, a specific, nontoxic small molecule Opa1 inhibitor identified in our laboratory (Pellattiero et al., 2019). The effects of MYLS22 on growth of implanted melanomas are fully dependent on endothelial Opa1, as confirmed by the lack of additive effects over Opa1 EC deletion. This proof of principle experiment indicate that Opa1 can be targeted in vivo by pharmacological means to counteract tumor growth. Indeed, OPA1 inhibition might be used to treat VEGFR-inhibitor-resistant tumors: by rewiring gene expression, *OPA1* inhibition downregulates the angiogenic factors (*FGFR*, *FGF*, *EGF*, *PDGF*) used by tumors escaping from VEGF inhibitors.

Our work identifies a previously unappreciated role for Opa1 in coordinating EC function and highlights the potential of OPA1 inhibition as an anticancer strategy, by counteracting tumor angiogenesis and metastatization.

Limitations of study.

One obvious limitation of our study is the lack of additional pre-clinical models of hematogenous metastasis. The classic model of experimental hematogenous metastasis reported here (tail vein injection) does not recapitulate all the steps of metastasis. The additional models of metastasis employed in this study depend on both hematogenous and lymphatic metastatization. A model of orthotopic implantation followed by resection would for example further clarify how EC Opa1 is required for the initial steps of metastatization.

STAR Methods

CONTACT FOR REAGENT AND RESOURCE SHARING

Further information and requests for resources and reagents should be directed to and will be fulfilled by the Lead Contact, Luca Scorrano (luca.scorrano@unipd.it)."

EXPERIMENTAL MODEL AND SUBJECT DETAILS

Mouse models

Animal housing and all the experimental procedures were authorized by the Italian Ministry of Health (383-2015-PR to LS). Mice were housed six per cage in a temperature (22-24°C) and humidity-controlled colony room, maintained on a 12-h light/dark cycle (07:00 to 19:00 light on), with standard food and water provided *ad libitum* and environmental enrichments. Endo-mito-EGFP mice were kindly provided by Dr. C. Vande Velde (Pickles et al., 2013). Cdh5(PAC)-CreERT2 mice were kindly provided by Dr. R.H. Adams (Wang et al., 2010), $P65^{f/f}$ by Dr. R.M. Schmid (Algul et al., 2007) and $Mfn1^{f/f}$ by Dr. A. Zorzano (Boutant et al., 2017). $Opa1^{+/\Delta EC}$ mice were generated by crossing $Opa1^{f/f}$ mice (Cogliati et al., 2013) with Tg(Tek-cre)2352Rwng (Tie2Cre) mice (Jackson's Laboratory). $Opa1^{i\Delta EC/i\Delta EC}$ were generated by crossing $Opa1^{f/f}$ mice with Cdh5(PAC)-CreERT2 mice. $Opa1^{f/f}::Opa1^{tg}$ mice were generated by crossing $Opa1^{f/f}$ with $Opa1^{tg}$ mice (Cogliati et al., 2013). The sequence of the primers used to genotype the mice are provided in Supplementary table S3.

For the retinal neovascularization model, sex of the pups was not considered. For BAPTA intraocular injection, animals were first allocated to different groups based on their genotype and then randomized for injection with BAPTA or DMSO. We analyzed

first the vessel coverage of the retina, then the branching points and finally the tip cells content. For the retinal vascularization model, we analyzed 8-12 pups per group and age; in the case of P4 $Opa1^{+/\Delta EC}$ and $Opa1^{f/+}$, we analyzed 21-25 pups.

For tumor experiments, we used 3-6 and 6-8-week-old females per group and we repeated each experiment twice. The allocation of mice in different group was based on their genotype. For *in vivo* matrigel experiment, we used 5-7 and 6-8-week-old males and we repeated the experiment twice. The allocation of mice in different group was based on their genotype. During all experiments, mice were monitored twice per day. Behavior, weight, furrow and tumor size were controlled every day. The total number of mice analyzed for each experiment is detailed in the figure legends.

Zebrafish models

Animal housing and all the experimental procedures were authorized by the Italian Ministry of Health (407/2015-PR to NT). Zebrafish (male and females) were housed twenty per thank (3.5 L) in a controlled water (temperature: 27-28°C, pH: 7.2-7.5, conductivity: 340-350 µs/cm, NO_2=0 mg/L, NO_3 50 mg/L, and maintained on a 12-h light/dark cycle (08:00 to 20:00 light on). Zebrafish were fed three times per day (2 times with dry food and once with artemia). Animals were maintained in tanks with environmental enrichment and mated in breeding tanks mimicking their natural reproductive habitat. Tg(*fli1a:EGFP*), Tg(*kdrl:mCherry*/*kdrl-mls:GFP)*, Tg(*stab1:YFP*), Tg(*kdrl:mCherry*) zebrafish (Zebrafish International Resource Center, ZIRC, Oregon, USA) were grown and subjected to *opa1* morpholino oligomers injections as previously described (Geudens et al., 2010).

Cell culture

All cells were grown at 37°C in a 5% CO_2 humid atmosphere. HUVECs (Lonza) were used from passages 3-9. Cells were seeded on 0.2% gelatin-coated dishes and maintained in culture in EGM-2 BulletKit medium (Lonza) supplemented with 5% fetal bovine serum (FBS). Experiments were performed in EGM2 medium supplemented when indicated with the VEGF (50ng/ml, Reliatech) or bFGF (10ng/ml, Promega).

Primary neonatal human dermal lymphatic microvascular endothelial cells (HMVEC-dLy) derived from a single donor (Lonza) were used from passages 1-7. Cells were seeded on 0.2% gelatin-coated dishes and maintained in EGM2-MV medium (Lonza).

MPECs were used from passages 2 to 3. Cells were seeded on 0.2% gelatin-coated-dishes and maintained in culture in EGM2 (Promocell).

B16F10 mouse melanoma cells (ATCC-CRL-6475) and MDA-MB-231 human breast adenocarcinoma cells (ATCC-HTB26) were cultured in DMEM supplemented with 10% fetal bovine serum (FBS), 100 U/ml penicillin and 100 µg/ml streptomycin.

E0771 mouse breast adenocarcinoma cells were cultured in DMEM 4500 supplemented with 10% FBS, 20mM Hepes pH 7.4, 100 U/ml penicillin and 100 µg/ml streptomycin.

Murine pulmonary microvascular endothelial cells isolation

MPECs were isolated as described (Sobczak et al., 2010). Lungs were digested with collagenase/dispase solution (Roche Applied Science) at a final concentration of 2 mg/ml for 45 min at 37°C. ECs were purified by using anti-PECAM-1 (CD31) (BD Pharmingen) antibody-conjugated Dynabeads for 15 min at room temperature. Finally,

beads were resuspended in EGM2 bullet kit (Lonza) medium and plated on gelatin coated dishes. When they reached 50% of confluence, a second purification step was performed using secondary anti-ICAM2 (BD Pharmingen)-conjugated Dynabeads (Invitrogen). MPECs were used between P2 and P4 for the different functional assays.

METHOD DETAILS

SiRNA transfection

180,000 cells per well in a 6-well plate; 80,000 cells per well in a 48-well plate and 8,000 cells per well in a 96-well plate were transfected with the following siRNAs: a non-relevant human sequence (*UNREL*) (AM4635, Ambion20 nM), *OPA1* (144409, Invitrogen 20 nM), *OPA1* siRNA2 (36409, Invitrogen; used as a control in not shown data), *P65* (40 nM), *MICU1* siRNA (50nM), *MFN1* (50 nM) and MFN2 (50 nM) using Dharmafect-4 (Dharmacon) according to manufacturer's instructions. All transfections experiments described in this paper were carried out with *MFN1* and *MFN2* siRNA1. Similar results were obtained with *MFN1* and *MFN*2 siRNA 2 (data not shown).

Functional assays on transfected HUVECs and evaluation of transfection efficiency were performed after 48 hours. HUVECs were trypsinized, stained with trypan blue and living cells were seeded for the different functional assays.

Cell proliferation Assay

HUVECs were transfected in a 96-well plate in 100µl EGM2 for 48 hours. The thymidine analogue 5-bromo-2-deoxyuridine (BrdU) was added and the culture was incubated for 16 hours. BrdU incorporation was measured with the Cell Proliferation ELISA BrdU

chemiluminescence kit (Roche Applied Science) according to the manufacturer's protocol.

Scratch wound migration assay

HUVECs were transfected in 48-well plate in 800 µL of EGM2 for 48 hours and were wounded with the head of a 200 µL tip. Migration of the cells into the wound was recorded 6 hours later.

Capillary network formation on a Matrigel matrix

5,000 HUVECs transfected as described above were plated in a 96-well plate pre-coated with 35 µl Matrigel per well (BD Biosciences) 48 hours post-transfection. Cells were incubated in EGM-2 medium for 5h (Lonza). Brightfield images were taken using a Leica DM4000 epifluorescence microscope equipped with 4X, 1.3 NA objectives. Quantitative analysis of network structure was performed with ImageJ software by counting the number of intersections in the network and measuring the total length of the structures.

NFκB binding activity

The P65 DNA-binding activity of NFκB was quantified by ELISA (EZ Transcription Factor Kit NFκB P65, Pierce) according to the manufacturer's instructions on total protein extracts. Protein concentration was determined using the BCA protein assay reagent (Pierce). NFκB binding to the target oligonucleotide was detected by incubation

with primary antibody specific for the activated form of P65, visualized by anti-IgG horseradish peroxidase conjugates and developing solution.

Calcium measurements

Cells were incubated at 37°C in Hank's balanced salt solution (HBSS, Sigma) containing 4% FBS and Fura2-AM (1 µM, Molecular Probes), pluronic acid 0.04% and sulfinpyrazione 250□M. After 30 min cells were trypsinized, pelleted at 1200 rpm for 3 minutes and resuspended in HBSS with 4%FBS (250,000 cells/experiment). Ratiometric Ca^{2+} measurements were performed at λ_{em}=340±5, 380±5 and λ_{ex}=510±15 nm at 37°C in a LS50B fluorimeter (Perkin Elmer) equipped with fast filter and magnetic stirring. Background was calculated as the average of 10 seconds fluorescence intensity at the beginning of the experiment, i.e. HBSS+4%FBS. Basal level refers to average Ratio of 10 timepoints (10s) upon addition of cells. The Ca^{2+}-ATPase inhibitor thapsigargin refers to average Ratio of 10 s at the plateau. R_{max}= average of 50 s upon reaching plateau. R_{min}: average of 50 s at the end of experiment. Thapsigargin was used at a final concentration of 10 µM.

Adenovirus infection

Acute *Opa1* ablation in *Opa1*$^{f/f}$ *Opa1*^{tg} MPEC was obtained by infection with adenoviruses expressing Cre-GFP (ad-CRE; 300 pfu; Vector Biolabs). GFP (ad-EV)-expressing adenoviruses were used as control at the same titer.

Western blotting

Cells were lysed in lysis buffer and heated at 95°C for 10 min. Equal amounts of protein were resolved by 8% SDS PAGE and transferred to polyvinylidene fluoride membranes (PVDF) according to the manufacturer's protocol. The blots were blocked for 1 hour at room temperature with 5% BSA (Sigma Aldrich) in Tris-buffered saline with 0.1% Tween 20 (TBS-T) and probed overnight at 4°C with 1:1000 primary antibody. After three washes with TBS-T, the appropriate secondary antibody at a 1:5000 dilution was added for 1 hour at room temperature. The bands were visualized by enhanced chemiluminescence ECL kit (Pierce).

Immunofluorescence

HUVECs ($3x10^5$) were cultured in 35-mm dishes coated with gelatin (0.2%). After VEGF (50 ng/ml) incubation, cells were washed with PBS, fixed with 4% paraformaldehyde for 15 min at room temperature, blocked and permeabilized with PBS-5%BSA-0.5% saponin solution, and incubated overnight in 1% PBS, 0.1% BSA-saponin (Sigma Aldrich) containing 1:100 primary antibody. After 3 washes with PBS cells were incubated with the same solution containing the corresponding secondary fluorescent antibodies Alexa Fluor 488 and 568 (Thermo Fisher Scientific) for 1 hour at room temperature. Samples were washed 3 times with PBS and nuclei were stained with DAPI. The samples were analyzed by confocal microscopy using the appropriate laser line of a LSM700 (Zeiss).

For immunofluorescence on tissues, cryostat sections (5 µm thick) were fixed in acetone at -20°C and in 100% methanol at 4°C and then incubated with rat monoclonal anti-PECAM-1 for 1 hour at room temperature. Slides were washed and incubated with

Alexa 488 anti-rat for 1h at 4°C. After three washes, slides were covered with coverslips in mounting medium (Victor Laboratories) and analyzed using a Leica DMI4000 microscope (equipped with 10X/0.25, 20X/0.35NA, 40X/0.6NA and 63X/1.25NA objectives).

Tamoxifen treatment

Tamoxifen injection in pups. To induce Tamoxifen-dependent ablation of *Opa1* in the endothelium, pups were injected intraperitoneally every day from P1 until P3 with 50 µl Tamoxifen (1mg/ml) (Sigma-Aldrich). Retinal vascularization and evaluation of the Opa1 deletion efficiency were performed from P5.

Tamoxifen injection in adult mice. Mice of 15-20-day old were injected intraperitoneally for five consecutive days with 100 µl Tamoxifen (10 mg/ml). Tumors, matrigel injection and evaluation of Opa1 deletion efficiency were performed on 6-week old mice.

Retinal murine neovascularization model

To analyze postnatal neovascularization in the mouse retina, *Opa1*$^{\Delta EC/+}$, *Opa1*$^{i\Delta EC}$, P65,*Opa1*$^{\Delta EC/+}$ and wild-type littermates were euthanized at the indicated postnatal day. Eyes were fixed in 4% paraformaldehyde (PFA) solution for 5 min, retinas were dissected and post-fixed in PFA 4% for 1 hour. After 5 washes with PBS, retinas were permeabilized in PBS with 1% BSA and 0.5% Triton overnight at 4°C. Retinas were then incubated with biotinylated isolectin B4 (Vector Laboratories) and mouse anti-Opa1 (BD-Biosciences) for 4 hours at 4°C and washed overnight in PBS. Secondary streptavidin–Alexa 488 (Invitrogen), anti-mouse Alexa 488 (1:300) were added for 2

hours at 4°C. The secondary antibody was washed overnight, and retinas were flat-mounted for the analysis conducted using Leica DMI4000 microscope (equipped with 2.5X/0.07NA, 5X/0.12NA, 10X/0.25NA, 20X/0.35NA, 40X/0.6NA and 63X/1.25NA objectives). Images were analyzed using ImageJ. The retinal radius (from the optic nerve to the edge of the retina) and the vascular radius (from the optic nerve to the vascular front) of each petal of the retina were measured. The vascular coverage was calculated as the ratio between the vascular radius and the retinal radius of each petal of a single retina. Branching were quantified using ImageJ. Images of tip cell's filopodia were taken by a confocal Zeiss LSM700 microscope (equipped with 10X/0.25, 20X/0.50NA, 40X/1.3NA and 63X/1.4NA objectives) and images were analyzed using ImageJ. For BAPTA experiments, pups were intraocularly injected at P1 with 5 mM/eye of BAPTA-AM or DMSO and sacrificed at P5.

Mouse tumor models

Opa1$^{+/\Delta EC}$, *Opa1*$^{i\Delta EC}$, *Opa1*$^{+/i\Delta EC}$, *P65,Opa1*$^{+/\Delta EC}$, *Mfn1*$^{i\Delta EC}$ and the corresponding control mice were used throughout the study.

Subcutaneous B16F10 melanoma model. Subconfluent B16F10 cells were trypsinized, washed and resuspended in PBS. B16F10 cell suspension ($5x10^4$ cells in 100µl PBS) was injected subcutaneously into the right flank of each mouse. Tumor growth of B16F10 cells was assessed by measuring the length and width of each tumor every day and calculating tumor volume by means of the formula: length x width^2 x 0.5. Sixteen days after tumor cells injection, the mice were euthanized, and their tumors harvested.

In case of subcutaneous B16F10 melanoma treated with MYLS22, mice were treated from day 10 after tumoral cells injection every two days with 10mg/kg/die MYLS22 resuspended in corn oil.

Mammary E0771 adenocarcinoma model. Subconfluent E0771 cells were trypsinized, washed and resuspended in PBS. E0771 cell suspension ($1.5x10^5$ cells in 100 µl PBS) was injected in the the fourth mammary gland in the lower abdomen of each mouse. Tumor growth of E0771 cells was assessed by measuring the length and width of each tumor every day and calculating tumor volume as described above. Twenty-two days after tumor cells injection, mice were euthanized, and their tumors harvested.

Footpad B16F10 melanoma model. 10^5 B16-F10 cells in 30 µl PBS were injected subcutaneously into the right hind footpad mice. Tumor growth was assessed by measuring the length and width of each tumor every day. Tumor volume was calculated as described above. Mice were euthanized, and tissues harvested 16 days after tumor inoculation.

Ear B16F10 melanoma model.10^6 B16-F10 cells in 40µl PBS were injected between the skin and cartilage on the dorsal side of the ear. Tumor growth was assessed by measuring the length and width of each tumor every two days. Tumor volume was calculated as described above. Mice were euthanized, and tissues harvested 30 days after tumor inoculation.

Matrigel plug assay

Matrigel (500µl) supplemented with 250ng/ml FGF2, 400ng/ml VEGF and 0.0025 Unit/ml heparin was implanted into mice under anesthesia in the right and left flank.

After 10 days, plugs were dissected from the mice and their weight were determined. Matrigels were ground in the presence of dispase solution (5mg/ml). The concentration of hemoglobin in the supernatant was determined directly by measuring the absorbance at 405 nm and compared with a standard curve of purified hemoglobin.

Zebrafish experimental treatments

For treatment with BAY 11-7082, embryos were placed in 12-well dishes (10-15 embryos per well, with random allocation for embryos that were subjected to Opa1 knockdown prior to control or inhibitor treatment). BAY 11-7082 (5 µm) or DMSO were added to the water at 12 hours post-fertilization (hpf).

Live screening and quantification of vascular abnormalities in the trunk were performed on Tricaine-anesthetized embryos (Sigma-Aldrich) at 24 hpf (ISV sprouting), 72 hpf (lymphatic vessels in Tg(*stab1:YFP*)) and 5 days post fertilization (Tg(*lyve1b:mCherry*)). Embryos were anaesthetized and positioned on a coverslip in a drop of 1% low melting point agarose. Imaging for vascular defects were performed using a Nikon confocal microscope Eclipse 90i (equipped with water immersion 20X/0.50NA and 40X/0.80NA objectives). Imaging for mitochondrial morphology were performed using a spinning disk Andromeda confocal microscope (FEI) using a 60X/1.35NA oil immersion objective.

Analysis of gene expression by qRT-PCR

RNAs were extracted with the miRNeasy kit (Qiagen) according to the manufacturer's protocol. cDNA synthesis was performed with 1 µg total RNA and the iScript cDNA Synthesis Kit (BioRad) according to the manufacturer's instructions. Resulting cDNAs

(20 ng) were used for quantitative real-time PCR using the SYBR green method (Roche Applied Sciences). Thermal cycling was performed on an ABI Prism 7900 HT Sequence Detection System (Applied Biosystems). For all reactions, no template controls were run, and random RNA preparations were also subjected to sham reverse transcription to check for the absence of genomic DNA amplification. Quantitative real-time PCR was performed with SYBR green method (Bioline and ThermoFisher Scientific). Thermal cycling was performed on an Applied Biosystem 7900 HT detection system and a Stratagene MX3005P multiplex QPCR system (Applied Biosystems and Stratagene).

The relative transcript level of each gene was normalized to the housekeeping genes cyclophilin-A (PPIA), beta-2 microglobulin (B2M) and/or GAPDH. Primers were designed using Primer Express software and selected to span exon-exon junctions to avoid detection of genomic DNA (primer sequences are provided in supplementary tables S1 and S2). Quantification of mRNA levels was calculated with the $2^{-\Delta Ct}$ method.

RNA sequencing experiment

RNA sequencing was performed by the GIGA Genomics Facility (Liège, Belgium). After 30h of transfection with 30 nM of Unrel or OPA1 siRNA, total RNA was isolated from HUVECs using RNeasy Mini Kit (Qiagen). Extracted RNA yields were determined using a NanoDrop® ND-1000 spectrophotometer (Thermo Fisher Scientific). The purity and quality of extracted RNAs were evaluated using the Experion RNA StdSens Analysis kit (Bio-Rad). High quality RNAs with RNA Quality Indicator (RQI) score greater than 8 were used for RNA sequencing experiments. Gene expression profiling was performed using An Illumina NextSeq500. For each sample, 250ng of total RNA were labeled

using an Illumina Total Prep RNA Amplification kit (Ambion) according to the manufacturer's instructions. The raw sequence reads were aligned by STAR (reference genome HOMO SAPIENS UCSChg19). The differential genes expression and their false discovery rate (FDR) corrected p values were calculated using *DESeq2* (*v*. *1.6.3*)

QUANTIFICATION AND STATISTICAL ANALYSIS

Data representation and Statistical analysis

Data are displayed as dot plots of at least three independent experiments. Plots include each datapoint, mean and SEM. In case of tumor growth curve, average±SEM is represented.

Statistical significance was calculated by a one-way ANOVA with Tukey's post-test. All P values and n are reported in the figure legends. Results are considered significant when $p<0.05$.

DATA AND SOFTWARE AVAILABILITY

Accession Number

RNA sequencing data have been deposited in GEO (accession #GSE122042).

KEY RESOURCES TABLE

REAGENT or RESOURCE	SOURCE	IDENTIFIER
Antibodies		
Rabbit anti-IκBα (C-21)	Santa Cruz Biotechnology	SC-371
Mouse anti-Opa1	BD-Biosciences	612607
rabbit anti-GRP75	Santa Cruz Biotechnology	sc-13967
Mouse anti-MICU1	Sigma Aldrich	#ACC-322
rabbit anti-P65	Cell Signalling Technology	8242
Rabbit anti-Tom20 (FL-145)	Santa Cruz Biotechnology	sc-11415
SDHA antibody	Abcam	ab14715
Rabbit anti-STAT3	Cell Signalling	4904
Rabbit anti-phospho-STAT3 (Tyr 705)	Cell Signalling	9131
Isolectin b4	Vector Laboratories	B1205
Rat anti mouse CD31	BD Pharmingen	550274
Anti mitofusin 1	NeuroMabs	75162
Anti mitofusin 2	ABM	Y401293
Anti-Actin-α-smooth muscle-CY3	Sigma Aldrich	C6198
Goat anti-esm1	R&D Systems	AF1999
Rat Anti-Mouse CD102	BD Pharmigen	553326
Goat anti-VEGFR2	R&D Systems	AF357
Rabbit anti GRP75	Santa Cruz	
Mouse anti-VE-Cadherin	BD-Biosciences	610251
Rabbit anti-ERK1/2-phospho, p44/42 MAPK Phospho	Cell Signaling Technology	9101
Rabbit anti-ERK1/2, p44/42 MAPK	Cell Signaling Technology	4695
Rabbit anti-AKT pan (11EZ)	Cell Signaling Technology	4685

Rabbit anti-AKT Phospho (Thr308) (C31E5E)	Cell Signaling Technology	2965
Rabbit anti-Phospho-Akt (Ser473) Antibody	Cell Signaling Technology	9271
Rabbit anti-CD11	Cell Signaling Technology	45581
Alexa Fluor 488 donkey anti goat IgG	Life Technologies	A11055
Alexa Fluor 488 goat anti mouse IgG	Life Technologies	A11029
Alexa Fluor 488 goat anti rabbit IgG	Life Technologies	A11070
Alexa Fluor 488 Chicken anti-Rat IgG	Life Technologies	A21470
Alexa Fluor 594 Donkey Anti-Goat IgG	Abcam	ab150136
Alexa Fluor 594 Donkey anti-Rabbit IgG	Thermo fisher	A10042
Alexa Fluor 568 Goat anti-Rat IgG	Thermo fisher	A-11077
Alexa Fluor 568 Goat anti-Mouse IgG	Thermo fisher	A-11019
Streptavidin Alexa Fluor 555 conjugate	Life Technologies	S21381
Streptavidin Alexa Fluor 488 conjugate	Life Technologies	S11223
Amersham ECL Mouse IgG, HRP-linked (sheep)	GE Healthcare	NA931
Amersham ECL Rabbit IgG, HRP-linked (donkey)	GE Healthcare	NA934
Bacterial and Virus Strains		
Biological Samples		
Chemicals, Peptides, and Recombinant Proteins		
VEGF165	Vinci-Biochem Srl	Rel 300-076
bFGF	Promega	G5071
BAY 11-7082	Calbiochem	A00308
BAPTA, AM	Thermo Fisher Scientific	B6769
LLL12	Sigma Aldrich	573131
AG490	Calbiochem	133550-30-8
PD98059	Calbiochem	167869-21-8

Sigma Aldrich	Sigma Aldrich	W1628
Evans Blue	Sigma-Aldrich	E2129
Fura-2, AM	Life Technologies	F1221
Tricaine	Sigma-Aldrich	A-5040
Rhodamine B	Sigma Aldrich	83689
Rotenone	Sigma-Aldrich	R8875-1G
FCCP	Sigma-Aldrich	C2920
Antimycin A	Sigma-Aldrich	A8674
Oligomycin	Sigma-Aldrich	O4876
TMRM	Invitrogen	T668
MYLS22	Enamine	EN300-333633
Thapsigargin	Sigma-Aldrich	T903
Heparin, endotoxin free	Sigma-Aldrich	2106
Collagenase, Dispase	Roche	10269638001
Dispase II	Sigma-Aldrich	D4693
Trypan Blue Solution, 0.4%	Thermo Fisher Scientific	15250061
Tamoxifen	Sigma-Aldrich	T5648-5G
Matrigel matrix 3D	VWR	7341100
Haemoglobin human	Sigma-Aldrich	H7379
Dharmafect 4	Dharmacon	T-2004-03
Critical Commercial Assays		
SensiMix Sybr NO-ROX Kit	Bioline	QT650-05
BrdU Chemiluminescence Kit	Roche	11647229001
EZ transcription Factor Kit NFκB P65	Pierce	89859
RNeasy Mini Kit	Qiagen	74104
Experion RNA StdSens Analysis kit	Bio-Rad	7007103

Pierce protein BCA assay	Thermo Fisher	23225
Annexin V-FITC Apoptosis Detection Kit	eBioscience	BMS500FI/300
Deposited Data		
RNA sequencing data	GEO	GSE122042
Experimental Models: Cell Lines		
HUVEC Pooled, in EGM™-2	Lonza	C2519A
HMVEC-dLy Ad, Adult	Lonza	CC-2810
Human Breast Adenocarcinoma MDA MB231	ATCC	ATCC-HTB26
Murine melanoma B16F10	ATCC	ATCC-CRL-6475
Mouse breast Adenocarcinoma E0771	Tebu-Bio	940001-A
Experimental Models: Organisms/Strains		
Endo-mito-EGFP mice	Pickles et al., 2013	N/A
Cdh5(PAC)-CreERT2 mice	Wang et al., 2010	N/A
P65$^{f/f}$ mice	Algul et al., 2007	
Tg(Tek-cre)2352Rwng (Tie2Cre) mice	Jackson's laboratory	008537
Opa1$^{f/f}$ mice	Cogliati et al., 2013	N/A
Opa1$^{\Delta EC/+}$ mice	This paper	N/A
Opa1$^{i\Delta EC}$ mice	This paper	N/A
Opa1^{tg} mice	Varanita et al., 2015	N/A
Opa1$^{f/f}$ Opa1^{tg} mice	This paper	N/A
Mfn1$^{i\Delta EC}$ mice	This paper.	N/A
Tg(*kdr*l:GFP) zebrafish	Liu et al., 2007	N/A
Tg(*kdrl*:mCherry) zebrafish	Wang et al., 2010	N/A
Tg(*kdrl:mCherry/kdrl-mls:GFP)* zebrafish	D. Stainier, MPI, Germany	N/A
Tg(*stab*:YFP) zebrafish	Hogan et al., 2009	N/A

Tg(*fli1a:*GFP) zebrafish	Lawson et al., 2002	N/A
Oligonucleotides		
siRNA		
OPA1 siRNA 1	Invitrogen	144409
OPA1 siRNA 2	Invitrogen	36409
Unrel	Ambion	AM4635
P65 siRNA 5'-GCC CUA UCC CUU UAC GUC AdTdT-3'	Halkein et al., 2013	N/A
SCR siRNA 5'-UCG ACC UCA CUU CCC AUU G-3'.	Halkein et al., 2013	N/A
MFN1 siRNA 1 5'-GGC GAU UAC UGC AAU CUU U-3',	De Brito et al., 2008	N/A
MFN1 siRNA2 5'-CCA GAU GAA CCU UUU AAC A-3'	De Brito et al., 2008	N/A
MFN2 siRNA1 5'-GGA GAG GGC CUU CAA GCG C-3'	De Brito et al., 2008	N/A
MFN2 siRNA2 5'-GAG ACA CAU GGC UGA GGU G-3'	De Brito et al., 2008	N/A
MICU1 siRNA 5'-GACUUCGCUUUACCCAAACAG-3'	Patron et al., 2014	N/A
Morpholino oligos		
opa1 translation blocking morpholino GATGAGTTTAGGATCTCTTTGCAGT	Rahn et al., 2013	N/A
unrel morpholino GATCACTTTACGATCTGTTTCCAGT	Rahn et al., 2013	N/A
Recombinant DNA		
Software and Algorithms		

Origin		
Corel Draw		
Image J		
RNA Express Version 1.1.0 Illumina Base Space		
Deseq2 version 1.6.3		
STAR		
Other		
EGM2 (Endothelial growth medium)	Promocell	C-22011
Endothelial cell growth factor supplements	Promocell	C-30120
Gelatin from bovine skin	SIgma aldrich	G9391
DMEM	Gibco	31885049
Penicillin-streptomycin (5000U/ml)	Invitrogen	15070-063
cOmplete™, Mini, EDTA-free Protease Inhibitor Cocktail	Roche	4693159001
PhosStop Phosphatase Inhibitor Cocktail Tablets	Roche	04906845001
Amersham Hybond 0.45um PVDF	Thermo Fisher Scientific	15407374
ExpressPlus PAGE Gel, 10x8, 8% 12 wells	GenScript	M00812
ExpressPlus PAGE Gel, 10x8, 4-12% 10 wells	GenScript	M41210
Trypsin-EDTA (0.25%)	Thermo Fisher	25200056
Bovine Serum Albumin	Sigma Aldrich	A8806
Zoletil 50	VIRBAC	7978320 6/2016
ROMPUN	BAYER HEALTHCARE	4222764 3/1980

Acknowledgments

We thank Dr. D. Stainier (MPI, Germany) for the *kdrl:mCherry/kdrl-mls:GFP* zebrafish lines and the Zebrafish facility from GIGA Research center (Liege, Belgium) for the Tg(*stab1:YFP*) zebrafish line. We thank Dr. M. Santoro (U. of Padua, Italy) for the Breast adenocarcinoma E0771 cells. We acknowledge the GIGA-genomics and Giga sequencing facilities (Liege, Belgium).

This work was supported by the Associazione Italiana per la Ricerca sul Cancro (AIRC) IG19991 and IG15748 (to LS) and IG19928 (to FA); European Research Council (ERC) FP7-282280 and European Union FP7 CIG PCIG13-GA-2013-618697; Ministero dell'Istruzione, dell'Università e della Ricerca (MIUR) FIRB RBAP11Z3YA_005 and PRIN 2017BF3PXZ (to LS); ERC H2020-725004 and CERCA Programme/Generalitat de Catalunya (to MC); European Foundation for the Study of Diabetes (EFSD)/Lilly Research grant (to MC and MG;. SAF2017-89116R-P (FEDER/EU) from MINECO (Spain) co-funded by European Regional Developmental Fund (ERDF), a Way to Build Europe (to MG). SH was supported by a FP7-Cofund DTI-IMPORT, an AIRC Fellowship, Fonds Léon Frédéricq (University of Liège) and by a Foundation Umberto Veronesi fellowship. AP is supported by an AIRC Fellowship.

Author contributions

S.H. performed experiments, analyzed and interpreted data. S.H. and L.S. conceived and designed experiments, discussed data, and wrote the manuscript. O.E., M.Z., M.C., A.P., G.P., M.G., G.D., A.A and E.N. contributed to experiments and data collection. G.S. performed bioinformatics analysis. T.G., D.S., C.B. provided materials and

reagents. F.A., A.V., N.T., M.S., E.Z., M.C and M.G. provided reagents and materials and discussed data. All authors revised the manuscript. L.S. supervised the project.

Declaration of Interests

LS and AP disclose that they are inventors of a submitted patent application by University of Padova and Veneto Institute of Molecular Medicine covering MYLS22 and its derivatives as Opa1 inhibitors. All other authors do not have competing interests.

References

Adams, R.H. (2003). Molecular control of arterial-venous blood vessel identity. Journal of anatomy *202*, 105-112.

Afolayan, A.J., Eis, A., Alexander, M., Michalkiewicz, T., Teng, R.J., Lakshminrusimha, S., and Konduri, G.G. (2016). Decreased endothelial nitric oxide synthase expression and function contribute to impaired mitochondrial biogenesis and oxidative stress in fetal lambs with persistent pulmonary hypertension. Am J Physiol Lung Cell Mol Physiol *310*, L40-49.

Agrawal, V., Maharjan, S., Kim, K., Kim, N.J., Son, J., Lee, K., Choi, H.J., Rho, S.S., Ahn, S., Won, M.H.*, et al.* (2014). Direct endothelial junction restoration results in significant tumor vascular normalization and metastasis inhibition in mice. Oncotarget *5*, 2761-2777.

Algul, H., Treiber, M., Lesina, M., Nakhai, H., Saur, D., Geisler, F., Pfeifer, A., Paxian, S., and Schmid, R.M. (2007). Pancreas-specific RelA/p65 truncation increases susceptibility of acini to inflammation-associated cell death following cerulein pancreatitis. J Clin Invest *117*, 1490-1501.

Ambati, B.K., Nozaki, M., Singh, N., Takeda, A., Jani, P.D., Suthar, T., Albuquerque, R.J., Richter, E., Sakurai, E., Newcomb, M.T.*, et al.* (2006). Corneal avascularity is due to soluble VEGF receptor-1. Nature *443*, 993-997.

Andras, I.E., Pu, H., Tian, J., Deli, M.A., Nath, A., Hennig, B., and Toborek, M. (2005). Signaling mechanisms of HIV-1 Tat-induced alterations of claudin-5 expression in brain endothelial cells. J Cereb Blood Flow Metab *25*, 1159-1170.

Bobek, V., Kolostova, K., Pinterova, D., Kacprzak, G., Adamiak, J., Kolodziej, J., Boubelik, M., Kubecova, M., and Hoffman, R.M. (2010). A clinically relevant, syngeneic model of spontaneous, highly metastatic B16 mouse melanoma. Anticancer Res *30*, 4799-4803.

Boutant, M., Kulkarni, S.S., Joffraud, M., Ratajczak, J., Valera-Alberni, M., Combe, R., Zorzano, A., and Canto, C. (2017). Mfn2 is critical for brown adipose tissue thermogenic function. EMBO J *36*, 1543-1558.

Carmeliet, P. (2005a). Angiogenesis in life, disease and medicine. Nature *438*, 932-936.

Carmeliet, P. (2005b). VEGF as a key mediator of angiogenesis in cancer. Oncology *69 Suppl 3*, 4-10.

Castellino, F.J., and Ploplis, V.A. (2005). Structure and function of the plasminogen/plasmin system. Thromb Haemost *93*, 647-654.

Chen, H., Detmer, S.A., Ewald, A.J., Griffin, E.E., Fraser, S.E., and Chan, D.C. (2003). Mitofusins Mfn1 and Mfn2 coordinately regulate mitochondrial fusion and are essential for embryonic development. J Cell Biol *160*, 189-200.

Chen, Y.H., Wu, H.L., Li, C., Huang, Y.H., Chiang, C.W., Wu, M.P., and Wu, L.W. (2006). Anti-angiogenesis mediated by angiostatin K1-3, K1-4 and K1-4.5. Involvement of p53, FasL, AKT and mRNA deregulation. Thromb Haemost *95*, 668-677.

Cipolat, S., Martins de Brito, O., Dal Zilio, B., and Scorrano, L. (2004). OPA1 requires mitofusin 1 to promote mitochondrial fusion. Proc Natl Acad Sci U S A *101*, 15927-15932.

Cipolat, S., Rudka, T., Hartmann, D., Costa, V., Serneels, L., Craessaerts, K., Metzger, K., Frezza, C., Annaert, W., D'Adamio, L.*, et al.* (2006). Mitochondrial rhomboid PARL regulates cytochrome c release during apoptosis via OPA1-dependent cristae remodeling. Cell *126*, 163-175.

Claxton, S., Kostourou, V., Jadeja, S., Chambon, P., Hodivala-Dilke, K., and Fruttiger, M. (2008). Efficient, inducible Cre-recombinase activation in vascular endothelium. Genesis (New York, NY : 2000) *46*, 74-80.

Cogliati, S., Frezza, C., Soriano, M.E., Varanita, T., Quintana-Cabrera, R., Corrado, M., Cipolat, S., Costa, V., Casarin, A., Gomes, L.C.*, et al.* (2013). Mitochondrial cristae shape determines respiratory chain supercomplexes assembly and respiratory efficiency. Cell *155*, 160-171.

Cruys, B., Wong, B.W., Kuchnio, A., Verdegem, D., Cantelmo, A.R., Conradi, L.C., Vandekeere, S., Bouche, A., Cornelissen, I., Vinckier, S.*, et al.* (2016). Glycolytic regulation of cell rearrangement in angiogenesis. Nature communications *7*, 12240.

Csordas, G., Golenar, T., Seifert, E.L., Kamer, K.J., Sancak, Y., Perocchi, F., Moffat, C., Weaver, D., de la Fuente Perez, S., Bogorad, R.*, et al.* (2013). MICU1 controls both the threshold and cooperative activation of the mitochondrial Ca(2)(+) uniporter. Cell Metab *17*, 976-987.

Cueni, L.N., and Detmar, M. (2008). The lymphatic system in health and disease. Lymphat Res Biol *6*, 109-122.

Dan, H.C., Cooper, M.J., Cogswell, P.C., Duncan, J.A., Ting, J.P., and Baldwin, A.S. (2008). Akt-dependent regulation of NF-{kappa}B is controlled by mTOR and Raptor in association with IKK. Genes Dev *22*, 1490-1500.

De Smet, F., Segura, I., De Bock, K., Hohensinner, P.J., and Carmeliet, P. (2009). Mechanisms of vessel branching: filopodia on endothelial tip cells lead the way. Arterioscler Thromb Vasc Biol *29*, 639-649.

Dobrina, A., and Rossi, F. (1983). Metabolic properties of freshly isolated bovine endothelial cells. Biochim Biophys Acta *762*, 295-301.

Elkin, M., and Vlodavsky, I. (2001). Tail vein assay of cancer metastasis. Curr Protoc Cell Biol *Chapter 19*, 19.12.11-19.12.17.

Forni, M.F., Peloggia, J., Trudeau, K., Shirihai, O., and Kowaltowski, A.J. (2016). Murine Mesenchymal Stem Cell Commitment to Differentiation Is Regulated by Mitochondrial Dynamics. Stem Cells *34*, 743-755.

Frezza, C., Cipolat, S., Martins de Brito, O., Micaroni, M., Beznoussenko, G.V., Rudka, T., Bartoli, D., Polishuck, R.S., Danial, N.N., De Strooper, B.*, et al.* (2006). OPA1 controls apoptotic cristae remodeling independently from mitochondrial fusion. Cell *126*, 177-189.

Fulop, L., Szanda, G., Enyedi, B., Varnai, P., and Spat, A. (2011). The effect of OPA1 on mitochondrial Ca(2)(+) signaling. PLoSONE *6*, e25199.

Gerhardt, H., Golding, M., Fruttiger, M., Ruhrberg, C., Lundkvist, A., Abramsson, A., Jeltsch, M., Mitchell, C., Alitalo, K., Shima, D.*, et al.* (2003). VEGF guides angiogenic sprouting utilizing endothelial tip cell filopodia. J Cell Biol *161*, 1163-1177.

Geudens, I., Herpers, R., Hermans, K., Segura, I., Ruiz de Almodovar, C., Bussmann, J., De Smet, F., Vandevelde, W., Hogan, B.M., Siekmann, A.*, et al.* (2010). Role of delta-like-4/Notch in the formation and wiring of the lymphatic network in zebrafish. Arterioscler Thromb Vasc Biol *30*, 1695-1702.

Gingras, D., Boivin, D., Deckers, C., Gendron, S., Barthomeuf, C., and Beliveau, R. (2003). Neovastat--a novel antiangiogenic drug for cancer therapy. Anticancer Drugs *14*, 91-96.

Guo, D., Wang, Q., Li, C., Wang, Y., and Chen, X. (2017). VEGF stimulated the angiogenesis by promoting the mitochondrial functions. Oncotarget *8*, 77020-77027.

Harjes, U., Bensaad, K., and Harris, A.L. (2012). Endothelial cell metabolism and implications for cancer therapy. Br J Cancer *107*, 1207-1212.

Harjes, U., Verfaillie, C., and Carmeliet, P. (2016). Endothelial Barrier and Metabolism: New Kids on the Block Regulating Bone Marrow Vascular Niches. Dev Cell *37*, 210-212.

Ikeda, Y., Aihara, K., Yoshida, S., Iwase, T., Tajima, S., Izawa-Ishizawa, Y., Kihira, Y., Ishizawa, K., Tomita, S., Tsuchiya, K.*, et al.* (2012). Heparin cofactor II, a serine protease inhibitor, promotes angiogenesis via activation of the AMP-activated protein kinase-endothelial nitric-oxide synthase signaling pathway. J Biol Chem *287*, 34256-34263.

Jiang, B., Xu, S., Hou, X., Pimentel, D.R., Brecher, P., and Cohen, R.A. (2004). Temporal control of NF-kappaB activation by ERK differentially regulates interleukin-1beta-induced gene expression. J Biol Chem *279*, 1323-1329.

Kanarek, N., London, N., Schueler-Furman, O., and Ben-Neriah, Y. (2010). Ubiquitination and degradation of the inhibitors of NF-kappaB. Cold Spring Harbor perspectives in biology *2*, a000166.

Kaplan, R.N., Riba, R.D., Zacharoulis, S., Bramley, A.H., Vincent, L., Costa, C., MacDonald, D.D., Jin, D.K., Shido, K., Kerns, S.A.*, et al.* (2005). VEGFR1-positive haematopoietic bone marrow progenitors initiate the pre-metastatic niche. Nature *438*, 820-827.

Kasahara, A., Cipolat, S., Chen, Y., Dorn, G.W., 2nd, and Scorrano, L. (2013). Mitochondrial fusion directs cardiomyocyte differentiation via calcineurin and Notch signaling. Science *342*, 734-737.

Kisanuki, Y.Y., Hammer, R.E., Miyazaki, J., Williams, S.C., Richardson, J.A., and Yanagisawa, M. (2001). Tie2-Cre transgenic mice: a new model for endothelial cell-lineage analysis in vivo. Dev Biol *230*, 230-242.

Kisseleva, T., Song, L., Vorontchikhina, M., Feirt, N., Kitajewski, J., and Schindler, C. (2006). NF-kappaB regulation of endothelial cell function during LPS-induced toxemia and cancer. J Clin Invest *116*, 2955-2963.

Kong, L.L., Yang, N.Z., Shi, L.H., Zhao, G.H., Zhou, W., Ding, Q., Wang, M.H., and Zhang, Y.S. (2017). The optimum marker for the detection of lymphatic vessels. Molecular and clinical oncology *7*, 515-520.

Krutzfeldt, A., Spahr, R., Mertens, S., Siegmund, B., and Piper, H.M. (1990). Metabolism of exogenous substrates by coronary endothelial cells in culture. J Mol Cell Cardiol *22*, 1393-1404.

Li, X., Tjwa, M., Moons, L., Fons, P., Noel, A., Ny, A., Zhou, J.M., Lennartsson, J., Li, H., Luttun, A.*, et al.* (2005). Revascularization of ischemic tissues by PDGF-CC via effects on endothelial cells and their progenitors. J Clin Invest *115*, 118-127.

Lilienbaum, A., and Israel, A. (2003). From calcium to NF-kappa B signaling pathways in neurons. Mol Cell Biol *23*, 2680-2698.

Lin, L., Hutzen, B., Li, P.K., Ball, S., Zuo, M., DeAngelis, S., Foust, E., Sobo, M., Friedman, L., Bhasin, D.*, et al.* (2010). A novel small molecule, LLL12, inhibits STAT3 phosphorylation and activities and exhibits potent growth-suppressive activity in human cancer cells. Neoplasia *12*, 39-50.

Luchsinger, L.L., de Almeida, M.J., Corrigan, D.J., Mumau, M., and Snoeck, H.W. (2016). Mitofusin 2 maintains haematopoietic stem cells with extensive lymphoid potential. Nature *529*, 528-531.

Lugus, J.J., Ngoh, G.A., Bachschmid, M.M., and Walsh, K. (2011). Mitofusins are required for angiogenic function and modulate different signaling pathways in cultured endothelial cells. J Mol Cell Cardiol *51*, 885-893.

Makino, A., Scott, B.T., and Dillmann, W.H. (2010). Mitochondrial fragmentation and superoxide anion production in coronary endothelial cells from a mouse model of type 1 diabetes. Diabetologia *53*, 1783-1794.

Mountain, D.J., Singh, M., Menon, B., and Singh, K. (2007). Interleukin-1beta increases expression and activity of matrix metalloproteinase-2 in cardiac microvascular endothelial cells: role of PKCalpha/beta1 and MAPKs. Am J Physiol Cell Physiol *292*, C867-875.

Nagy, J.A., Chang, S.H., Dvorak, A.M., and Dvorak, H.F. (2009). Why are tumour blood vessels abnormal and why is it important to know? Br J Cancer *100*, 865-869.

Ou, J.J., Wei, X., Peng, Y., Zha, L., Zhou, R.B., Shi, H., Zhou, Q., and Liang, H.J. (2015). Neuropilin-2 mediates lymphangiogenesis of colorectal carcinoma via a VEGFC/VEGFR3 independent signaling. Cancer Lett *358*, 200-209.

Paltauf-Doburzynska, J., Malli, R., and Graier, W.F. (2004). Hyperglycemic conditions affect shape and Ca2+ homeostasis of mitochondria in endothelial cells. J Cardiovasc Pharmacol *44*, 423-436.

Patten, I.S., and Arany, Z. (2012). PGC-1 coactivators in the cardiovascular system. Trends Endocrinol Metab *23*, 90-97.

Pellattiero, A., Quirin, C., Herkenne, S., Biris, N., Cendron, L., Gavathiotis, E., and Scorrano, L. (2019). A high throughput screening identifies a small molecule inhibitor of OPA1 that enhances apoptotic release of cytochrome c and sensitizes cancer cells to treatment. Submitted.

Pernas, L., Bean, C., Boothroyd, J.C., and Scorrano, L. (2018). Mitochondria Restrict Growth of the Intracellular Parasite Toxoplasma gondii by Limiting Its Uptake of Fatty Acids. Cell Metab *27*, 886-897 e884.

Pernas, L., and Scorrano, L. (2016). Mito-Morphosis: Mitochondrial Fusion, Fission, and Cristae Remodeling as Key Mediators of Cellular Function. Annu Rev Physiol *78*, 505-531.

Phng, L.K., and Gerhardt, H. (2009). Angiogenesis: a team effort coordinated by notch. Dev Cell *16*, 196-208.

Pickles, S., Cadieux-Dion, M., Alvarez, J.I., Lecuyer, M.A., Peyrard, S.L., Destroismaisons, L., St-Onge, L., Terouz, S., Cossette, P., Prat, A.*, et al.* (2013). Endo-MitoEGFP mice: a novel transgenic mouse with fluorescently marked mitochondria in microvascular endothelial cells. PLoS One *8*, e74603.

Pierce, J.W., Schoenleber, R., Jesmok, G., Best, J., Moore, S.A., Collins, T., and Gerritsen, M.E. (1997). Novel inhibitors of cytokine-induced IkappaBalpha phosphorylation and endothelial cell adhesion molecule expression show anti-inflammatory effects in vivo. J Biol Chem *272*, 21096-21103.

Popov, D., and Simionescu, M. (2006). Cellular mechanisms and signalling pathways activated by high glucose and AGE-albumin in the aortic endothelium. Archives of physiology and biochemistry *112*, 265-273.

Potente, M., and Carmeliet, P. (2017). The Link Between Angiogenesis and Endothelial Metabolism. Annual Review of Physiology *79*, 43-66.

Potente, M., Gerhardt, H., and Carmeliet, P. (2011). Basic and therapeutic aspects of angiogenesis. Cell *146*, 873-887.

Qiu, J., Wang, G., Peng, Q., Hu, J., Luo, X., Zheng, Y., Teng, Y., and Tang, C. (2011). Id1 induces tubulogenesis by regulating endothelial cell adhesion and cytoskeletal organization through beta1-integrin and Rho-kinase signalling. Int J Mol Med *28*, 543-548.

Ribeiro, A.L., and Okamoto, O.K. (2015). Combined effects of pericytes in the tumor microenvironment. Stem cells international *2015*, 868475.

Roberts, D.M., Kearney, J.B., Johnson, J.H., Rosenberg, M.P., Kumar, R., and Bautch, V.L. (2004). The vascular endothelial growth factor (VEGF) receptor Flt-1 (VEGFR-1) modulates Flk-1 (VEGFR-2) signaling during blood vessel formation. Am J Pathol *164*, 1531-1535.

Sales, G., Calura, E., Cavalieri, D., and Romualdi, C. (2012). graphite - a Bioconductor package to convert pathway topology to gene network. BMC bioinformatics *13*, 20.

Seo, I.A., Lee, H.K., Shin, Y.K., Lee, S.H., Seo, S.Y., Park, J.W., and Park, H.T. (2009). Janus Kinase 2 Inhibitor AG490 Inhibits the STAT3 Signaling Pathway by Suppressing Protein Translation of gp130. The Korean journal of physiology & pharmacology : official journal of the Korean Physiological Society and the Korean Society of Pharmacology *13*, 131-138.

Shenouda, S.M., Widlansky, M.E., Chen, K., Xu, G., Holbrook, M., Tabit, C.E., Hamburg, N.M., Frame, A.A., Caiano, T.L., Kluge, M.A., *et al.* (2011). Altered mitochondrial dynamics contributes to endothelial dysfunction in diabetes mellitus. Circulation *124*, 444-453.

Simons, M., and Eichmann, A. (2013). Physiology. Lymphatics are in my veins. Science *341*, 622-624.

Sobczak, M., Dargatz, J., and Chrzanowska-Wodnicka, M. (2010). Isolation and culture of pulmonary endothelial cells from neonatal mice. Journal of visualized experiments : JoVE.

Soler, A.P., Marano, C.W., Bryans, M., Miller, R.D., Garulacan, L.A., Mauldin, S.K., Stamato, T.D., and Mullin, J.M. (1999). Activation of NF-kappaB is necessary for the restoration of the barrier function of an epithelium undergoing TNF-alpha-induced apoptosis. Eur J Cell Biol *78*, 56-66.

Stahl, A., Connor, K.M., Sapieha, P., Chen, J., Dennison, R.J., Krah, N.M., Seaward, M.R., Willett, K.L., Aderman, C.M., Guerin, K.I.*, et al.* (2010). The mouse retina as an angiogenesis model. Invest Ophthalmol Vis Sci *51*, 2813-2826.

Tabruyn, S.P., Sorlet, C.M., Rentier-Delrue, F., Bours, V., Weiner, R.I., Martial, J.A., and Struman, I. (2003). The antiangiogenic factor 16K human prolactin induces caspase-dependent apoptosis by a mechanism that requires activation of nuclear factor-kappaB. Mol Endocrinol *17*, 1815-1823.

Tadros, A., Hughes, D.P., Dunmore, B.J., and Brindle, N.P. (2003). ABIN-2 protects endothelial cells from death and has a role in the antiapoptotic effect of angiopoietin-1. Blood *102*, 4407-4409.

Tarca, A.L., Draghici, S., Khatri, P., Hassan, S.S., Mittal, P., Kim, J.S., Kim, C.J., Kusanovic, J.P., and Romero, R. (2009). A novel signaling pathway impact analysis. Bioinformatics *25*, 75-82.

Tomar, D., Thomas, M., Garbincius, J.F., Kolmetzky, D.W., Salik, O., Jadiya, P., Carpenter, A.C., and Elrod, J.W. (2019). MICU1 regulates mitochondrial cristae structure and function independent of the mitochondrial calcium uniporter channel. bioRxiv, 803213.

Tsien, R.Y. (1980). New calcium indicators and buffers with high selectivity against magnesium and protons: design, synthesis, and properties of prototype structures. Biochemistry *19*, 2396-2404.

Valle, I., Alvarez-Barrientos, A., Arza, E., Lamas, S., and Monsalve, M. (2005). PGC-1alpha regulates the mitochondrial antioxidant defense system in vascular endothelial cells. Cardiovasc Res *66*, 562-573.

Varanita, T., Soriano, M.E., Romanello, V., Zaglia, T., Quintana-Cabrera, R., Semenzato, M., Menabo, R., Costa, V., Civiletto, G., Pesce, P.*, et al.* (2015). The OPA1-dependent mitochondrial cristae remodeling pathway controls atrophic, apoptotic, and ischemic tissue damage. Cell Metab *21*, 834-844.

Wang, Y., Nakayama, M., Pitulescu, M.E., Schmidt, T.S., Bochenek, M.L., Sakakibara, A., Adams, S., Davy, A., Deutsch, U., Luthi, U.*, et al.* (2010). Ephrin-B2 controls VEGF-induced angiogenesis and lymphangiogenesis. Nature *465*, 483-486.

Wilczynska, K.M., Gopalan, S.M., Bugno, M., Kasza, A., Konik, B.S., Bryan, L., Wright, S., Griswold-Prenner, I., and Kordula, T. (2006). A novel mechanism of tissue inhibitor

of metalloproteinases-1 activation by interleukin-1 in primary human astrocytes. J Biol Chem *281*, 34955-34964.

Wilkinson, D.G. (2001). Multiple roles of EPH receptors and ephrins in neural development. Nature reviews Neuroscience *2*, 155-164.

Wu, Z.B., Cai, L., Lin, S.J., Leng, Z.G., Guo, Y.H., Yang, W.L., Chu, Y.W., Yang, S.H., and Zhao, W.G. (2016). Heat Shock Protein 47 Promotes Glioma Angiogenesis. Brain Pathol *26*, 31-42.

Xiao, Q.G., Liu, Z.G., Zhang, M., Zheng, J.L., Zhang, Z.H., Luo, L.H., and Chen, J.Q. (2005). [Effect of doxycycline on inflammation-related cytokines and apoptosis in human conjunctival epithelial cells]. Zhonghua Yan Ke Za Zhi *41*, 842-846.

Zecchin, A., Kalucka, J., Dubois, C., and Carmeliet, P. (2017). How Endothelial Cells Adapt Their Metabolism to Form Vessels in Tumors. Frontiers in immunology *8*, 1750.

Figure legends

Figure 1: Mitochondria elongate during angiogenesis.

(A) Representative confocal image of intersomitic vessels (ISVs) of zebrafish Tg(*kdrl:mCherry/kdrl-mls:GFP*) at 24 hpf showing blood vessels (red) and endothelial mitochondria (green). Scale bar: 100 µm.

(B) Representative confocal GFP imaging of living flat-mounted retinas from adult *Endo-MitoEGFP* mouse showing mitochondria in blood vessels. Scale bar: 150 µm.

(C-D) Representative GFP imaging of living stalk and tip endothelial cells in flat-mounted retinas extracted from Endo-MitoEGFP mouse at P4. Scale bar: 150 µm.

(E) Box plot of mitochondrial length in experiments as in C,D. Each dot represents 1 mitochondrion (n=50, 3 independent mice). *: $p=5x10^{-15}$ adult vs. stalk cells; $p=2x10^{-11}$ tips vs. stalk cells.

(F) Representative confocal images of mitochondrial morphology in HUVEC treated for 1h as indicated and stained for TOM20. Scale bar: 30 µm.

(G) Box plot of mitochondrial length in experiments as in F. Each dot represents 1 mitochondrion, n=3 independent experiments. *: $p=4x10^{-14}$ untreated vs. VEGF.

(H) Heat map of transcriptional changes measured by RNA sequencing during VEGF treatment (1,4 and 12h) of HUVEC. Data are resorted from http://angiogenes.uni-frankfurt.de and elaborated as detailed in the text.

(I) Average±SEM of 3 independent experiments of *OPA1*, *MFN1* and *MFN2* mRNA levels in HUVEC treated with VEGF (50 ng/ml) as indicated. *: $p<0.05$.

(J) Equal amounts of protein from HUVEC treated where indicated with VEGF (50 ng/ml) were separated by SDS-PAGE and immunoblotted with the indicated antibodies.

(K) Schematic representation of late retinal vascular development. In this model, from P7 onwards the superficial vascular plexus (L1) and blood vessels sprout to form the deeper layer (L3).

(L) Representative confocal image vascular layer 1, stained for OPA1 (green) and isolectin b4 (red) showing blood vessels from WT mice at P6. F represents the forefront where tip cells are located. Scale bar: 100 µm.

(M) Representative confocal images of vascular layer 1 (L1, quiescent ECs) and 3 (L3, angiogenic ECs) of retina extracted from WT mice at P11, fixed and stained for OPA1 (green) and isolectin b4 (red) to mark blood vessels. Scale bar: 150 µm.

Figure 2: *Opa1* is required for angiogenesis *in vitro* and *in vivo*.

(A) Representative isolectin b4 immunofluorescence (magnification 2.5x) of flat-mounted retinas from 5-day-old pups of the indicated genotype. Scale bar: 50 µm.

(B) Quantification of radial expansion. Experiments were performed as in (B). *: p=0.005, n=5 mice.

(C) Representative brightfield images acquired at the indicated time points of MPEC from 4-day old pups of indicated genotype in a scratch-wound assay. Scale bar: 250 µm.

(D) Quantification of cellular migration after 6h in experiments as in (C). n=6 independent experiments, n>4 mice per genotype. *: p=0.008.

(E) Quantification of proliferation of MPEC extracted from 4-day old pups of indicated genotype determined by BrdU incorporation. n=4 independent experiments, n>4 mice per group. *: $p=6x10^{-5}$.

(F) Representative isolectin b4 immunofluorescence (magnification 2.5x) of flat-mounted retinas from 4-day-old pups of the indicated genotype. a (red) indicates the radius of vascular front and b (yellow) the radius of retina. Scale bar: 50 µm.

(G) Quantification of radial expansion calculated as the ratio between the radius of vascular front (a) and the radius of retina (b). Experiments were as in (F). *: $p=5x10^{-12}$; n=21 *Opa1*$^{f/+}$ and 25 *Opa1*$^{+/\Delta EC}$ mice.

(H) Representative isolectin-b4 immunofluorescence (magnification 5x) of flat-mounted retinas showing blood vessels and branching points from 4-day-old pups of the indicated genotype. Scale bar: 100 µm.

(I) Quantification of branching points/mm^2 of retina. Experiments were performed as in (H). *: $p=3x10^{-6}$; n=11 *Opa1*$^{f/+}$ and 10 *Opa1*$^{+/\Delta EC}$ mice.

(J) Representative isolectin b4 immunofluorescence (magnification 40x) of flat-mounted retinas from 4-day-old pups of the indicated genotype. Red arrows mark tips cells. Scale bar: 20 µm.

(K) Quantification of tip cells number. Experiments were performed as in (J). *: $p=5x10^{-5}$; n=10 *Opa1*$^{f/+}$ and 8 *Opa1*$^{+/\Delta EC}$ mice.

(L) Representative isolectin b4 immunofluorescence (magnification 2.5x) of flat-mounted retinas from 6-day-old pups of the indicated genotype injected with tamoxifen at P1-P3. a (red) indicates the radius of vascular front and b (yellow) the radius of retina. Scale bar: 50 µm.

(M) Quantification of radial expansion calculated as the ratio between the radius of vascular front (a) and the radius of retina (b) in experiments as in (L). *: $p= 4x10^{-5}$; n=10 *Opa1*$^{f/f}$ and 11 *Opa1*$^{i\Delta EC}$ mice.

(N) Representative isolectin b4 immunofluorescence (magnification 5x) of flat-mounted retinas showing blood vessels and branching points in 6-day-old pups of the indicated genotype. Scale bar: 100 µm.

(O) Quantification of branching points/mm^2 of retina. Experiments were performed as in (N) in 6-day-old pups of the indicated genotype. *: p=8x10^{-6}; n=11 *Opa1$^{f/f}$* and 11 *Opa1$^{i\Delta EC}$* mice.

(P) Representative isolectin b4 immunofluorescence (magnification 40x) of flat-mounted retinas showing blood vessels and tips cells (red arrows) from 6-day-old pups of the indicated genotype. Scale bar: 20 µm.

(Q) Quantification of number of tip cells. Experiments were performed as in (P) from 6-day-old pups of the indicated genotype. *: p=2x10^{-7}; n=10 mice/genotype.

(R) Equal amounts of protein from zebrafish injected for 48h with *opa1* morpholino as indicated were separated by SDS-PAGE and immunoblotted with the indicated antibodies.

(S) Representative confocal images of endothelial mitochondria in intersomitic vessels of *Tg(kdrl:mls:GFP)* zebrafish 24h post injection with the indicated morpholino. Scale bar: 100µm.

(T) Quantification of mitochondria length in intersomitic blood vessel of zebrafish injected with the indicated morpholinos. Each dot represents 1 mitochondrion. n=40 mitochondria from 3 independent experiments. *: *P*=2x10^{-9} *unrel* vs. *opa1*.

(U) Representative confocal images of sprouting of intersomitic vessels (ISV) of Tg(*fli1a:GFP*) zebrafish 30h after injection with the indicated morpholino. Scale bar: 100 µm.

(V) Quantification of number of ISVs sprouts (black) and filopodia length (blue) in experiments as in (U). *: $p=4x10^{-5}$ (number); n=12 *unrel* and 14 *opa1* morphants; *: $p=8x10^{-5}$ (length); n=15 *unrel* and 16 *opa1* morphants.

(W) Representative photographs of Matrigel plugs implanted 8 days in 6-week-old mice of the indicated genotype. Scale bar: 0.3 cm.

(X) Quantification of hemoglobin content in Matrigel plug. Experiments were performed as in (W). *: $p= 8x10^{-6}$; n=14 $Opa1^{f/+}$ and 10 $Opa1^{+/\Delta EC}$ mice.

Figure 3: Opa1 orchestrates NFκB signaling and angiogenic gene expression.

(A) $2^{\Delta ct}$ of *OPA1* mRNA levels determined by RT-PCR in HUVEC treated as indicated. *: $p<0.05$; n=3 independent experiments.

(B) $Opa1^{f/f}::Opa1^{tg}$ MPEC were infected with the indicated adenoviruses and after 48 hrs treated where indicated for 10 minutes with VEGF (50ng/mL) and lysed. Equal amounts of protein (40 µg) were separated by SDS-PAGE and immunoblotted with the indicated antibodies.

(C) $Opa1^{f/f}::Opa1^{tg}$ MPEC were infected with the indicated adenoviruses and after 48h treated where indicated with VEGF for 6h. Cellular migration was quantified at 6h in a scratch wound assay. *: $p<0.05$; n=6 independent experiments.

(D) $Opa1^{f/f}::Opa1^{tg}$ MPEC were infected with the indicated adenoviruses and after 48h treated where indicated with VEGF for 24h. Cellular proliferation was quantified by measuring BrdU incorporation after 24h. *: $p<0.05$; n= 3 independent experiments.

(E) Total cellular ATP levels were measured in HUVEC transfected for 48h with the indicated siRNA as indicated (n=20 independent experiments) and in MPEC isolated from P4 pups of the indicated genotype (n=12 mice/condition).

(F) Volcano plot of differentially expressed genes in HUVEC transfected for 32h with siRNA against *OPA1* or a non-relevant sequence (*UNREL*). Red and green dots correspond to genes down-regulated and upregulated in Opa1-ablated HUVECs. n=3 independent experiments.

(G) Average±SEM of expression levels of the indicated genes in HUVEC transfected for 32h with *OPA1* siRNA determined by RT-PCR in 4 independent experiments. *: $p<0.05$.

(H) Bubble plot of pathway perturbation vs. over-representation from the RNAseq experiments. The graph plots the -log10 of the p-values of the two types of evidence computed by iPathwayGuide: over-representation (pORA) and total pathway accumulation (pAcc). Each pathway is represented by a single bubble, whose size is proportional to pathway representation. Red: significantly altered pathways; yellow: significantly altered pathways involving NFκB proteins regulators.

(I) Fold changes of genes involved in the NFκB pathway in HUVEC transfected with *OPA1* siRNA compared to *UNREL* siRNA. Experiment is performed as in (G). n=3 independent experiments.

(J) HUVEC were transfected with the indicated siRNA and after 48h the P65 DNA-binding ability was determined by a specific ELISA. *: p=0.02; n=6 independent experiments.

(K) HUVEC were transfected with the indicated siRNA and after 48h treated where indicated with VEGF (50ng/ml). The P65 DNA-binding ability was determined by a specific ELISA. *: $p<0.05$; n=3 independent experiments.

(L) Equal amounts of protein extracted from HUVEC transfected 48h with siRNA as indicated were separated by SDS-PAGE and immunoblotted with the indicated antibodies.

(M) *Opa1*$^{f/f}$ MEFs were infected with the indicated adenovirus and after 48hrs mitochondria were isolated and protein complexes were separated BN-PAGE, transferred onto a PVDF membrane, and probed with the indicated antibodies. The boxed area highlights the reduced MICU1-MCU-Opa1 containing complex.

(N) Quantification of Fura-2 Ratio (proportional to cytosolic Ca^{2+} levels) in HUVEC transfected for 48h with the indicated siRNAs. *: p=0.001 *UNREL vs. OPA1;* p=0.02 *UNREL vs. MICU1*; p=0.04 *UNREL vs. OPA1, MICU1*; n=4 independent experiments. NS: not significant.

(O) Equal amounts of protein extracted from HUVEC transfected 48h with the indicated siRNA and treated with BAPTA (1 mM) for 8h as indicated were separated by SDS-PAGE and immunoblotted with the indicated antibodies.

(P) HUVEC were transfected with the indicated siRNA and after 48h treated where indicated with BAPTA (1mM) for 8h. The P65 DNA-binding ability was determined by a specific ELISA. *: p=0.0003 *UNREL* vs. *OPA1*; #: p=0.002 *OPA1,DMSO* vs. *OPA1,BAPTA*; n=5 independent experiments

(Q) Representative brightfield images at the indicated time points of a scratch-wound assay using HUVEC transfected with the indicated siRNA for 48h and treated as indicated. Scale bar: 100µm.

(R) Quantification of cellular migration at 6h in experiments as in Q. *: $p<0.05$; n=6 independent experiments.

(S) Representative isolectin b4 immunofluorescence (magnification 2.5x) of flat-mounted retinas from 5-day-old pups of the indicated genotype treated where indicated with BAPTA-AM (5mM) delivered by intravitreal injection at P1. Scale bar: 50µm.

(T, U) Quantification of radial expansion (T) and branching points (U) in experiments as in S. *: $p=3x10^{-5}$ (T) and $2x10^{-5}$ (U) *Opa1*$^{f/+}$-vehicle vs *Opa1*$^{+/\Delta EC}$-vehicle; #: $p=1x10^{-6}$ (T) and 0.003 (U) *Opa1*$^{+/\Delta EC}$-vehicle vs. *Opa1*$^{+/\Delta EC}$-BAPTA. n=10 *Opa1*$^{f/+}$-vehicle, 8 *Opa1*$^{+/\Delta EC}$-vehicle and *Opa1*$^{f/+}$-BAPTA, 7 *Opa1*$^{+/\Delta EC}$-BAPTA mice.

Figure 4: OPA1 ablation impairs angiogenesis by activating NF□B.

(A) Representative brightfield images acquired at the indicated time points of scratch wound assays of HUVEC transfected for 48h with the indicated siRNA. Scale bar: 100 µm.

(B) Quantification of cellular migration after 6h in experiments as in (C). *: $p=6x10^{-5}$ *UNREL,SCR* vs *SCR,OPA1*; #: $p=5x10^{-5}$ *SCR,OPA1* vs. *P65,OPA1;* n=6 independent experiments.

(C) Representative brightfield images of endothelial tubular network in HUVEC transfected with the indicated siRNA and seeded on Matrigel for 6h. Scale bar: 200 µm.

(D) Quantification of branching points in experiments as in C. *: p=0.001 *UNREL,SCR* vs *SCR,OPA1*; #: p=0.0021 *SCR,OPA1* vs. *P65,OPA1*; n=7 independent experiments.

(E) Quantification of tube length o in experiments as in C. *: $p=7x10^{-6}$ *UNREL,SCR* vs *SCR,OPA1*; #: $p=1x10^{-10}$ *SCR,OPA1* vs. *P65,OPA1*; n=6 independent experiments.

(F) Representative isolectin b4 immunofluorescence (magnification 2.5x) of flat-mounted retinas showing blood vessels from 6-day-old pups of the indicated genotype injected with tamoxifen at P1-P3. a (red) indicates the radius of vascular front and b (yellow) the radius of retina. Scale bar: 50 µm.

(G) Quantification of radial expansion calculated as the ratio between the radius of vascular front (a) and the radius of retina (b) in experiments as in (F). *: $p=1x10^{-6}$ $Opa1^{f/+}$ vs. $Opa1^{+/\Delta EC}$; #: p=0.01 $Opa1^{+/\Delta EC}$ vs. $P65,Opa1^{+/\Delta EC}$; n=7 $P65^{f/+}$, 9 $P65^{+/\Delta EC}$, 8 $P65,Opa1^{f/+}$, 18 $P65,Opa1^{+/\Delta EC}$, 13 $Opa1^{f/+}$ and 7 $Opa1^{+/\Delta EC}$ mice.

(H) Quantification of branching points/mm^2 of retina. Experiments were performed as in F in 5-day-old pups of the indicated genotype. *: $p=6x10^{-5}$ $Opa1^{f/+}$ vs. $Opa1^{+/\Delta EC}$, #: $p=2x10^{-7}$ $Opa1^{+/\Delta EC}$ vs. $P65,Opa1^{+/\Delta EC}$; n=5 $P65^{f/+}$, $P65^{+/\Delta EC}$ and $P65,Opa1^{f/+}$, 9 $P65,Opa1^{+/\Delta EC}$, 8 $Opa1^{f/+}$ and 6 $Opa1^{+/\Delta EC}$ mice.

(I) Quantification of total venous branching points/mm of vein. Experiments were performed as in F in 5-day-old pups of the indicated genotype. *: $p=3x10^{-5}$ $Opa1^{f/+}$ vs. $Opa1^{+/\Delta EC}$, #: $p=2x10^{-5}$ $Opa1^{+/\Delta EC}$ vs. $P65,Opa1^{+/\Delta EC}$; n=5 $P65^{f/+}$, 7 $P65^{+/\Delta EC}$, 8 $P65,Opa1^{f/+}$, 12 $P65,Opa1^{+/\Delta EC}$, 10 $Opa1^{f/+}$ and 11 $Opa1^{+/\Delta EC}$ mice.

(J) Quantification of distal venous branching points. Experiments were performed as in F from 5-day-old pups of the indicated genotype. *: $p=2x10^{-5}$ $Opa1^{f/+}$ vs. $Opa1^{+/\Delta EC}$; #:

p=5x10^{-6} *Opa1*$^{+/\Delta EC}$ vs. *P65,Opa1*$^{+/\Delta EC}$; n=7 *P65*$^{f/+}$, 11 *P65*$^{+/\Delta EC}$, 10 *P65,Opa1*$^{f/+}$, 14 *P65,Opa1*$^{+/\Delta EC}$, 12 *Opa1*$^{f/+}$ and *Opa1*$^{+/\Delta EC}$ mice.

(K) Representative confocal images of sprouting of intersomitic vessels (ISV) of zebrafish Tg(*fli1a:GFP*) showing blood vessels at 30h post morpholino injection and treated as indicated. Scale bar: 100 µm.

(L) Quantification of number of ISV filopodia. Experiments were performed as in K. *: p=2x10^{-6} *unrel*-DMSO vs. *opa1*-DMSO; #: p=3x10^{-7} *opa1*-DMSO vs. *opa1*-BAY11-7082; n=11 *unrel*, 18 *opa1*, 9 *unrel*-BAY11-7082 and 14 *opa1*-BAY11-7082 zebrafishes.

(M) Quantification of filopodia length of ISV. Experiments were performed as in K. *: p=1x10^{-4} *unrel*-DMSO vs. *Opa1*-DMSO; #: p=2x10^{-5} *opa1*-DMSO vs. *opa1*-BAY11-7082; n=6 *unrel*, n=10 *opa1*, n=5 *unrel*-BAY11-7082 and n=7 *opa1*-BAY11-7082 zebrafishes.

(N) Representative brightfield images acquired at the indicated time points of scratch wound assays of HUVEC transfected for 48h with the indicated siRNA. Scale bar: 100 µm.

(O) Quantification of cellular migration after 6h in experiments as in (N). *: p<0.05, n=8 independent experiments.

(P) Representative brightfield images of endothelial tubular network in HUVEC transfected with the indicated siRNA and seeded on Matrigel for 6h. Scale bar: 250 µm.

(Q) Quantification of branching points in experiments as in P. *: p<0.05, n=5 independent experiments.

(R) Quantification of tube length in experiments as in P. *: p<0.05, n=5 independent experiments.

(S) Quantification of cellular proliferation as determined by BrdU incorporation after 24h in HUVEC transfected for 48h with the indicated siRNA. *: $p<0.05$; n=6 independent experiments.

Figure 5: EC *Opa1* deletion or inhibition curtails tumor growth

(A) Photographs of representative melanomas removed after 16 days from subcutaneous implants of $5x10^4$ B16F10 cells in 6-week-old mice of the indicated genotype. Scale bar: 0.5 cm.

(B) Growth curves of subcutaneously implanted $5x10^4$ B16F10 melanomas at day 0 in 6-week-old mice of the indicated genotype. n=7 $Opa1^{f/+}$ and 9 $Opa1^{+/\Delta EC}$ mice. *: $p<0.05$.

(C) Representative CD31 immunofluorescence (red) showing blood vessels in B16F10 melanomas in experiments as in A. Scale bar: 100 µm.

(D, E) Quantification of tumor blood vessels diameter (D) and surface per field (E) in experiments as in C.*: p=0.005 (D) and 0.009 (E). n=7 $Opa1^{f/+}$ and 9 $Opa1^{+/\Delta EC}$ mice.

(F) Representative photographs of melanomas removed after 16 days from the subcutaneous implants of $5x10^4$ B16F10 cells in 6-week-old mice of the indicated genotype. Scale bar: 0.5 cm.

(G) Growth curves of $5x10^4$ B16F10 melanoma cells subcutaneously implanted at day 0 in 6-week-old mice of the indicated genotype. n=7 $Opa1^{f/+}$ and $Opa1^{f/f}$, 9 $Opa1^{+/i\Delta EC}$ and $Opa1^{i\Delta EC}$ mice. *: $p<0.05$.

(H) Representative CD31 immunofluorescence (red) showing blood vessels in B16F10 melanomas in experiments as in G. Scale bar: 100 µm.

(I,J) Quantification of tumor blood vessels diameter (I) and surface per field (J) in experiments as in C.*: p<0.05. n=8 *Opa1$^{f/f}$* and 9 *Opa1$^{i\Delta EC}$* mice.

(K) Representative photographs of melanomas removed after 16 days from subcutaneous implants of 5x10^4 B16F10 cells in 6-week-old mice of the indicated genotype. Scale bar: 0.5 cm.

(L) Growth curves of 5x10^4 B16F10 melanoma cells subcutaneously implanted at day 0 in 6-week-old mice of the indicated genotype. *: p<0.05 n=11 *P65$^{f/+}$*, 8 *P65$^{+/\Delta EC}$*, *P65,Opa1$^{f/+}$*, *Opa1$^{f/+}$* and *Opa1$^{+/\Delta EC}$*, 12 *P65,Opa1$^{+/\Delta EC}$* mice.

(M) Photographs of representative melanomas removed after 16 days from subcutaneous implants of 5x10^4 B16F10 cells in 6-week-old mice of the indicated genotype. Mice were treated where indicated with MYLS22 or DMSO (10mg/kg) by peritumoral injection in sunflower oil (final V: 50 µl) every two days from day 10. Scale bar: 0.5 cm.

(N) Growth curves of subcutaneously implanted B16F10 (5x10^4) tumors in 6-week-old mice of the indicated genotype treated as indicated. n=5 mice/group. *: p<0.05.

Figure 6: EC *Opa1* deletion impairs tumor metastatization

(A) Photographs of lungs containing metastases from tail vein injected melanomas. Eleven days before mice were euthanized, organs explanted and images acquired, B16F10 (50x10^3) cells injected in the tail vein in 6-week-old mice of the indicated genotype. Scale bar: 1 cm.

(B) Quantification of macro-metastases in lung. Experiments were performed as in (A). *p<0.0005, n=6 *Opa1$^{f/+}$* and 8 *Opa1$^{+/\Delta EC}$* mice.

(C) Photographs of representative 6-week-old mice of the indicated genotype 14 days after the injection of $1x10^5$ melanoma B16F10 cells in the footpad.

(D) Growth curves of footpad implanted $1x10^5$ B16F10 melanomas at day 0 in 6-week-old mice of the indicated genotype. n=14 *Opa1*$^{f/+}$ and 8 *Opa1*$^{+/\Delta EC}$ mice. *: $p<0.05$.

(E) Photographs of representative sentinel popliteal lymph nodes explanted from mice of the indicated genotype in experiments as in A. Metastases of B16F10 melanomas are visible as dark masses. Scale bar: 0.5 cm.

(F) Photographs of representative 6-week-old mice of the indicated genotype 14 days after the injection of $1x10^5$ melanoma B16F10 cells into the footpad.

(G) Growth curves of footpad implanted $1x10^5$ B16F10 melanomas at day 0 in 6-week-old mice of the indicated genotype. n=14 *Opa1*$^{f/+}$ and 8 *Opa1*$^{i\,\Delta EC}$ mice. *: $p<0.05$.

(H) Photographs of representative sentinel popliteal lymph nodes explanted from mice of the indicated genotype in experiments as in E. Metastases of B16F10 melanomas are visible as dark masses. Scale bar: 0.5 cm.

(I) Representative confocal images of CD31 (red) and DAPI (blue) immunofluorescence showing blood vessels in B16F10 melanomas from experiments as in F. Note the DAPI$^+$ melanoma cells in the tumor vessels of *Opa1*$^{f/+}$ but not of *Opa1*$^{i\,\Delta EC}$ mice.

(J) Representative confocal images of CD31 immunofluorescence (red) in melanomas explanted from the footpad of mice of the indicated genotype 16 days after the injection of $5x10^4$ B16F10 cells. Scale bar: 100 µm.

(K-M) Quantification of number of tumor blood vessels per field (K), tumor blood vessels diameter (L) and tumor blood vessels surface per field (M) in experiments as in F. *: $p=0.002$ in (L) and $p=8x10^{-6}$ in (M). n=14 *Opa1*$^{f/f}$ and 8 *Opa1*$^{i\Delta EC}$ mice.

(N) Representative confocal images of Hoechst (nuclei, blue) CD31 (endothelial marker, green) and SMA (pericyte marker, red) immunofluorescence in experiments as in F. Scale bar: 250 µm.

(O) Photographs of ears of 6-week-old mice of the indicated genotype 30 days after the injection of $5x10^5$ melanoma B16F10 cells. Scale bar: 0.5 cm.

(P) Quantification of tumor size in the ear. Experiment was performed as in (I). n=11 *Opa1*$^{f/+}$ and 8 *Opa1*$^{+/\Delta EC}$ mice.

(Q) Photographs of representative sentinel cervical lymph nodes explanted from mice of the indicated genotype in experiments as in (I). Metastases of B16F10 melanomas are visible as dark masses. Scale bar: 0.5 cm.

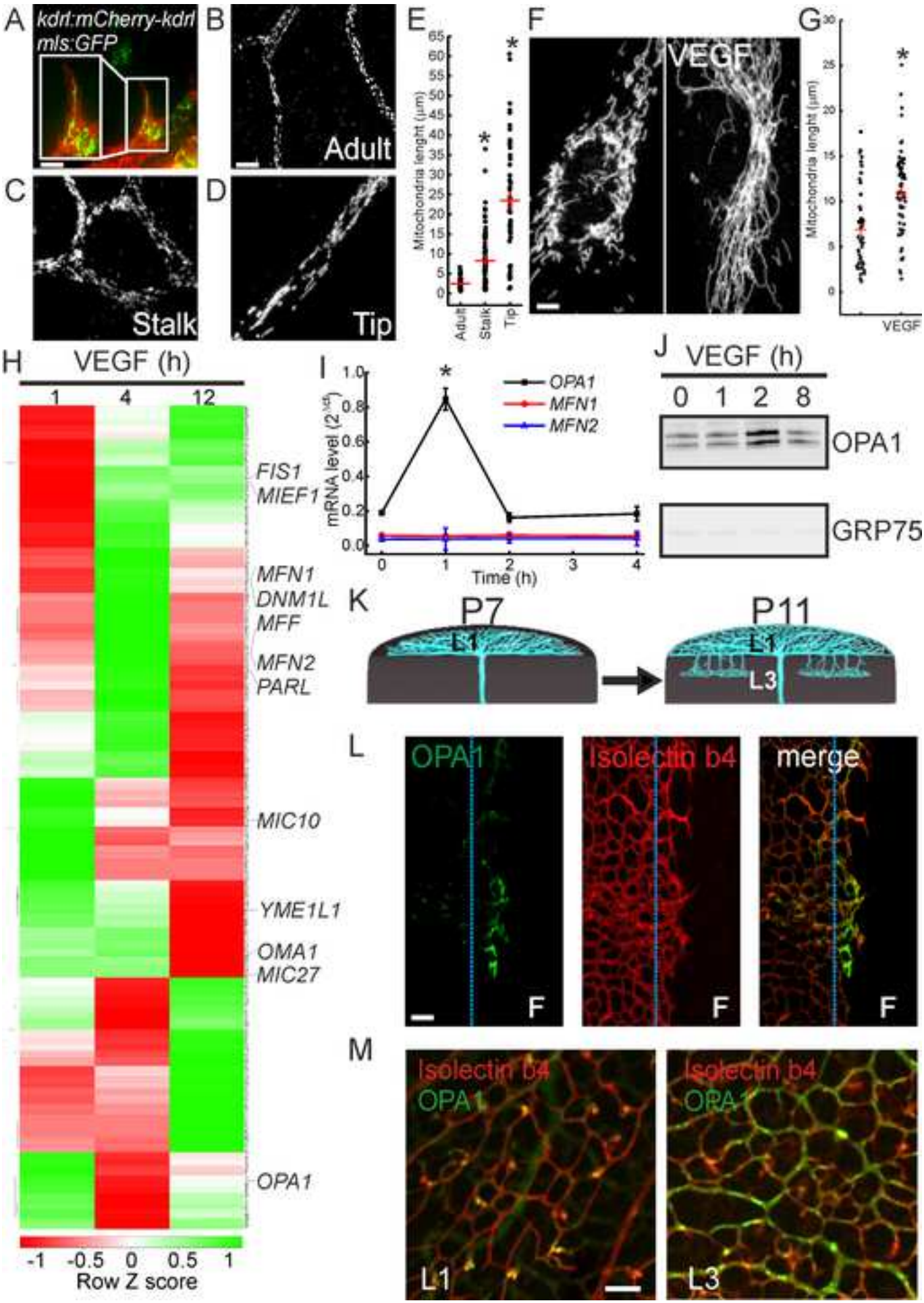

Fig 2

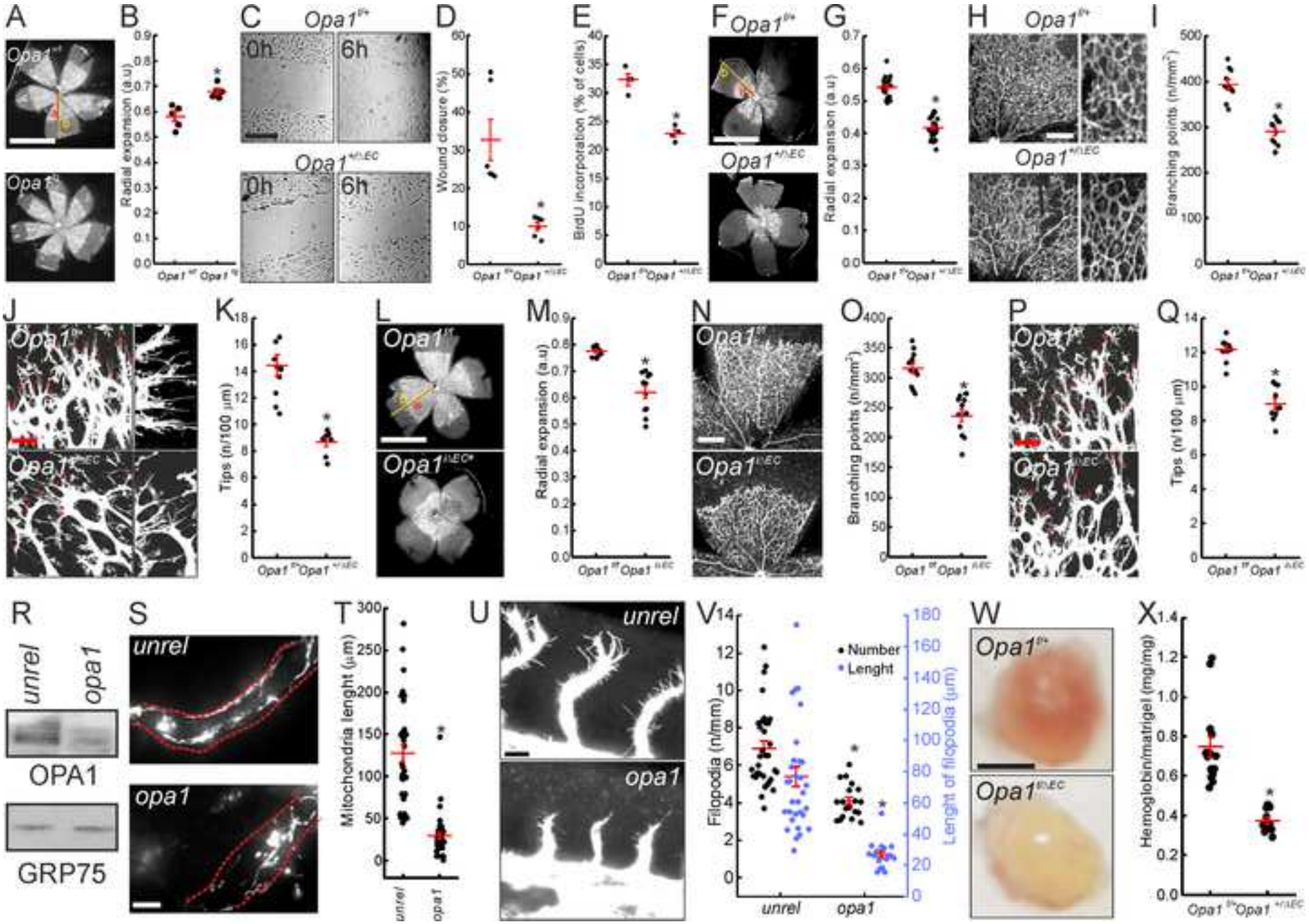
A
Opa1
Opa1
B
Radial expansion (a.u)
0.9
0.8
0.7
0.6
0.5
0.4
0.3
0.2
0.1
0.0
Opa1
Opa1
C
Opa1
0h
6h
Opa1
0h
6h
D
Wound closure (%)
60
50
40
30
20
10
0
Opa1
Opa1
E
BrdU incorporation (% of cells)
40
35
30
25
20
15
10
5
0
Opa1
Opa1
F
Opa1
Opa1
G
Radial expansion (a.u)
0.7
0.6
0.5
0.4
0.3
0.2
0.1
0.0
Opa1
Opa1
H
Opa1
Opa1
I
Branching points (n/mm²)
500
400
300
200
100
0
Opa1
Opa1
J
Opa1
Opa1
K
Tips (n/100 μm)
18
16
14
12
10
8
6
4
2
0
Opa1
Opa1
L
Opa1
Opa1
M
Radial expansion (a.u)
0.9
0.8
0.7
0.6
0.5
0.4
0.3
0.2
0.1
0.0
Opa1
Opa1
N
Opa1
Opa1
O
Branching points (n/mm²)
400
350
300
250
200
150
100
50
0
Opa1
Opa1
P
Opa1
Opa1
Q
Tips (n/100 μm)
14
12
10
8
6
4
2
0
Opa1
Opa1
R
unrel
opa1
OPA1
GRP75
S
unrel
opa1
T
Mitochondria lenght (μm)
300
250
200
150
100
50
0
unrel
opa1
U
unrel
opa1
V
Filopodia (n/mm)
14
12
10
8
6
4
2
0
Number
Lenght
Lenght of filopodia (μm)
180
160
140
120
100
80
60
40
20
0
unrel
opa1
W
Opa1
Opa1
X
Hemoglobin/matrigel (mg/mg)
1.4
1.2
1.0
0.8
0.6
0.4
0.2
0.0
Opa1
Opa1
*

Fig 3

Click here to access/download;Figure;Figure 3.tif

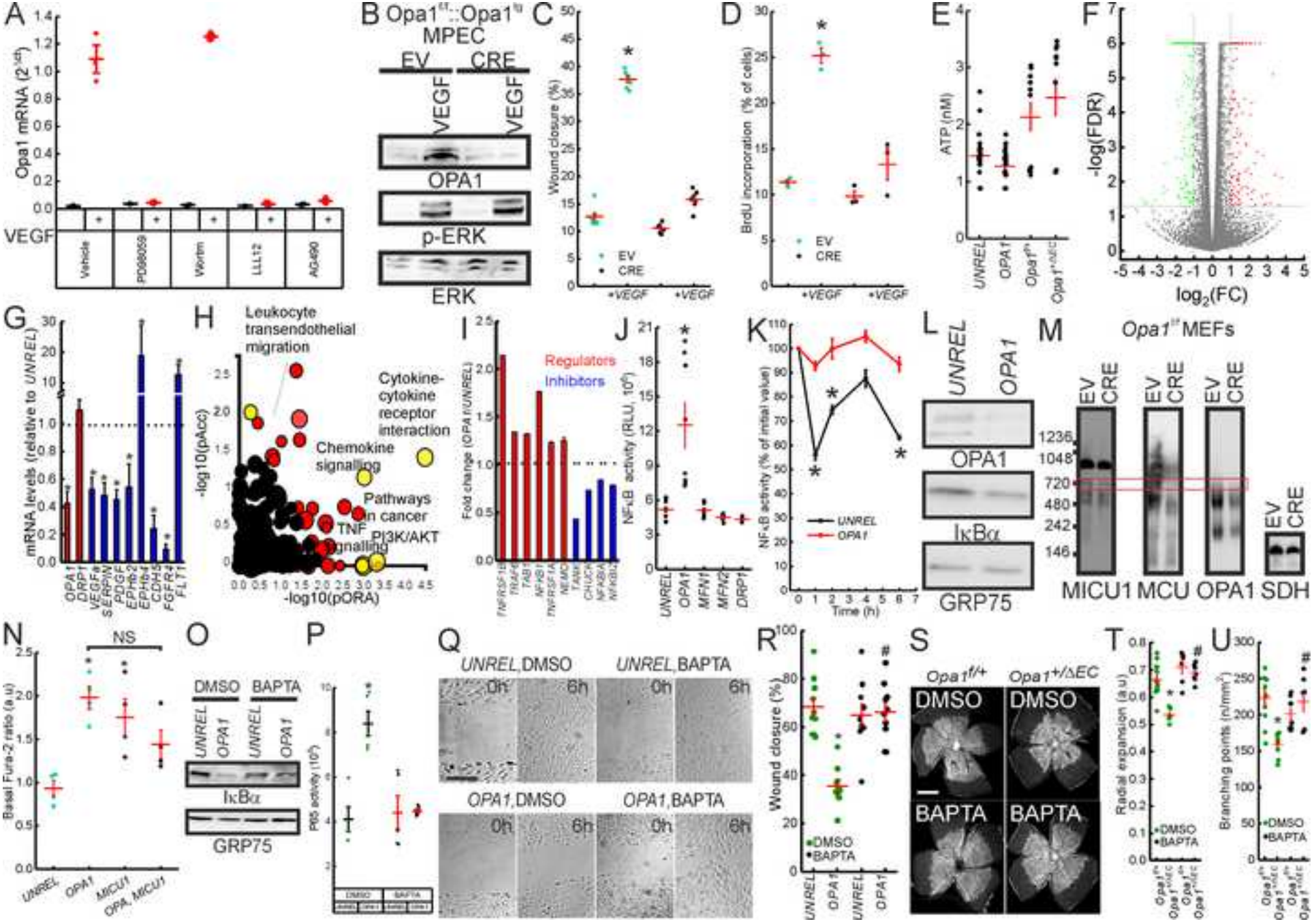

Fig 4

Click here to access/download;Figure;Figure 4.tif

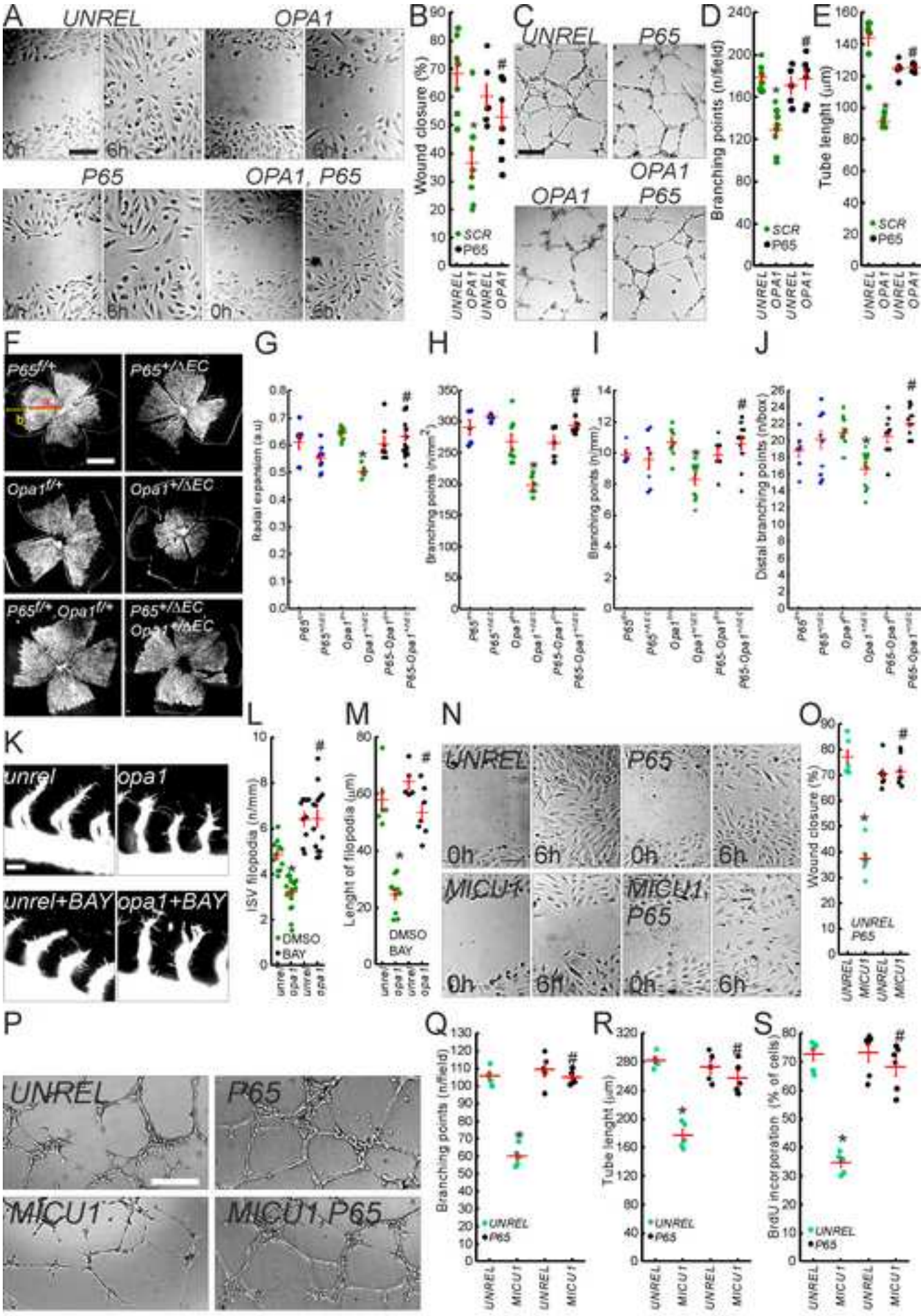

Fig 5

Click here to access/download;Figure;Figure 5.tif

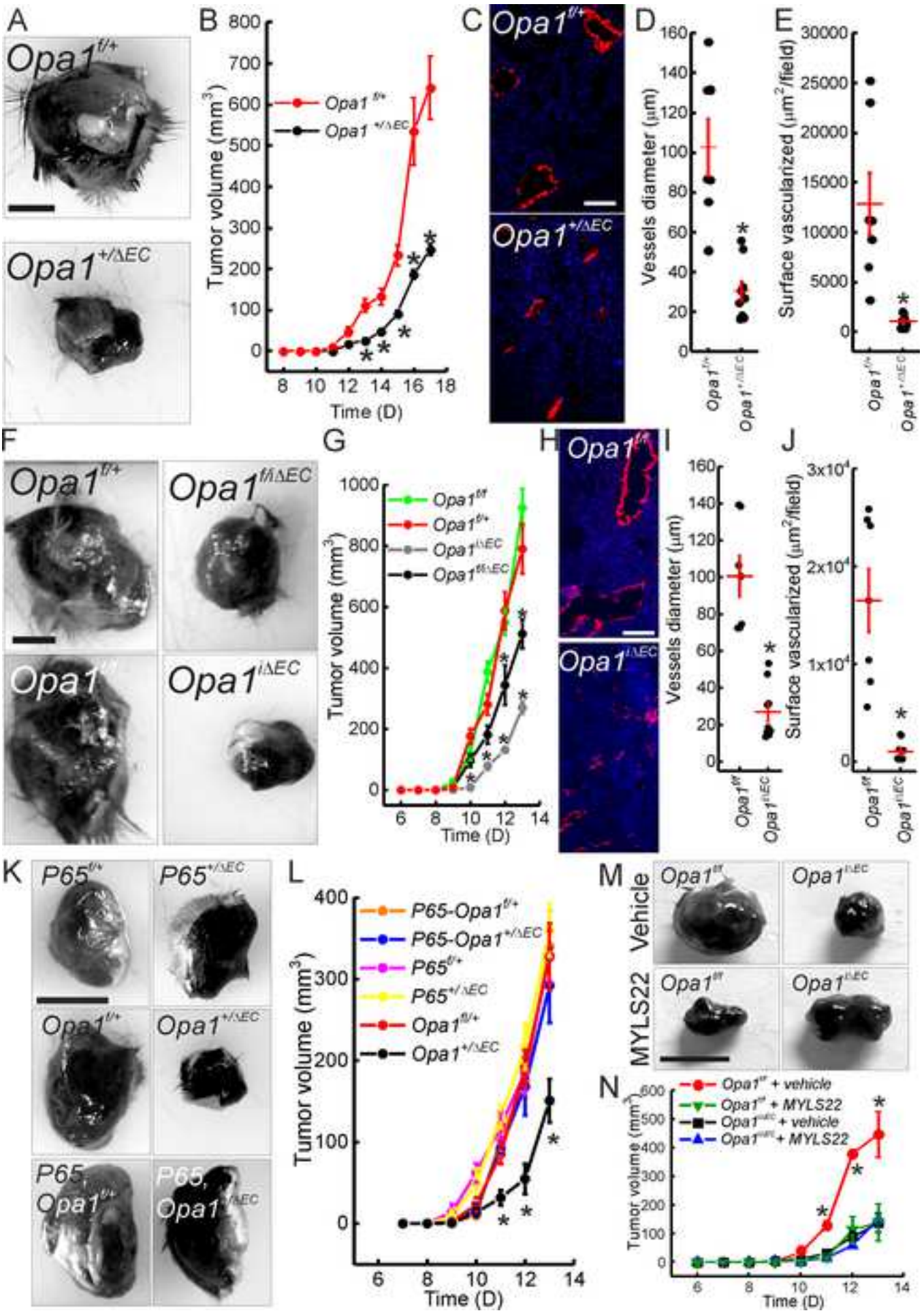

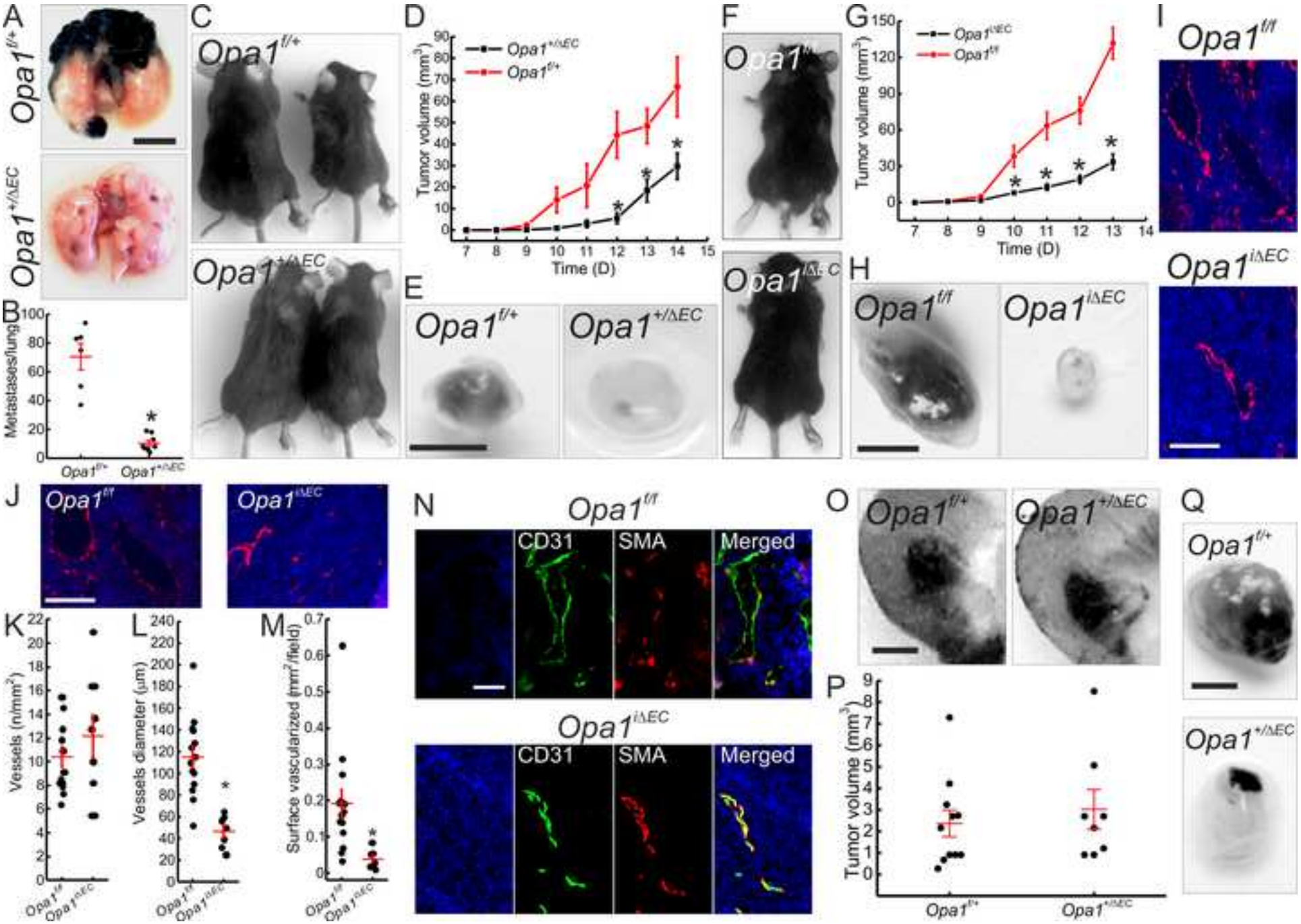

Developmental and tumour angiogenesis requires the mitochondria-shaping protein Opa1.

Herkenne et al.

Supplementary online material

Supplementary Figures

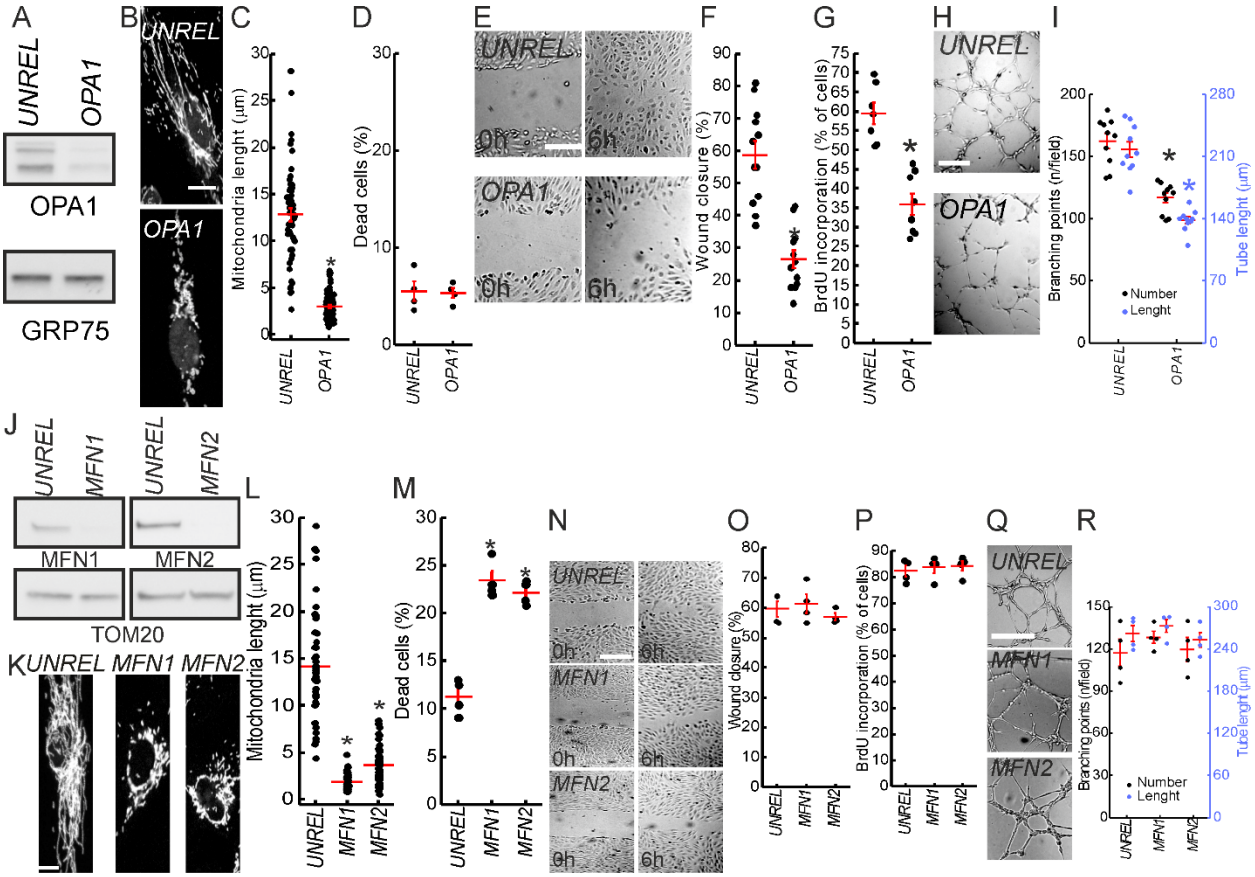

Supplementary Figure 1: *OPA1* but not mitofusins silencing affects angiogenesis in HUVEC, related to Fig. 2

(A) Equal amounts of protein from HUVEC transfected for 48h as indicated were separated by SDS-PAGE and immunoblotted with the indicated antibodies.

(B) Representative confocal images of mitochondrial morphology in HUVEC transfected 48h as indicated as indicated and stained for TOM20.

(C) Quantification of mitochondrial length in HUVEC transfected for 48h with indicated siRNA. Each dot represents 1 mitochondrion. *: $p=3x10^{-18}$. n=3.

(D) Quantification of cell death determined by Annexin/PI staining in HUVEC transfected for 48h with indicated siRNA. n=4.

(E) Representative brightfield images of HUVEC transfected with the indicated siRNA for 48h in a scratch-wound assay. Scale bar: 100µm.

(F) Quantification of cellular migration determined by scratch wound assay at 6h in experiments as in E. *$p=5x10^{-6}$, n=12.

(G) Quantification of cellular proliferation determined by measuring BrdU incorporation after 24h in HUVEC transfected for 48h with indicated siRNA. *$p=3x10^{-5}$, n=7.

(H) Representative brightfield images of endothelial tubular network of HUVEC transfected with the indicated siRNA seeded on Matrigel for 6h. Scale bar: 250 µm.

(I) Quantification of branching points (black) and tube length (blue) in experiments as in H. *: $p=1x10^{-5}$ (number), $p=2x10^{-6}$ (length). n=10.

(J) Equal amounts of protein extracted from HUVEC transfected 48h with the indicated siRNA were separated by SDS-PAGE and immunoblotted with the indicated antibodies.

(K) Representative confocal images of mitochondrial morphology in HUVEC transfected for 48h with the indicated siRNA and stained for TOM20. Scale bar: 30 µm.

(L) Quantification of mitochondrial length in experiments as in K. Each dot represents 1 mitochondrion. *: $p=1x10^{-21}$ *UNREL* vs *MFN1;* $p=4x10^{-19}$ *UNREL* vs *MFN2.* n=3.

(M) Quantification of cell death determined by Annexin/PI staining in HUVEC transfected for 48h with indicated siRNA. n=4. *: $p=1x10^{-4}$.

(N) Representative brightfield images of a scratch wound assay with HUVEC transfected for 48h with the indicated siRNA. Scale bar: 100 µm.
(O) Quantification of cellular migration at 6h in a scratch wound assay in experiments as in N. n=4.
(P) quantification of cellular proliferation determined by measuring BrdU incorporation after 24h in HUVEC transfected for 48h with indicated siRNA. n=4.
(Q) Representative brightfield images of endothelial tubular network of HUVEC transfected with the indicated siRNA seeded on Matrigel for 6h. Scale bar: 250 µm.
(R) Quantification of branching points (black) and tube length (blue) in experiments as in Q. n=4.

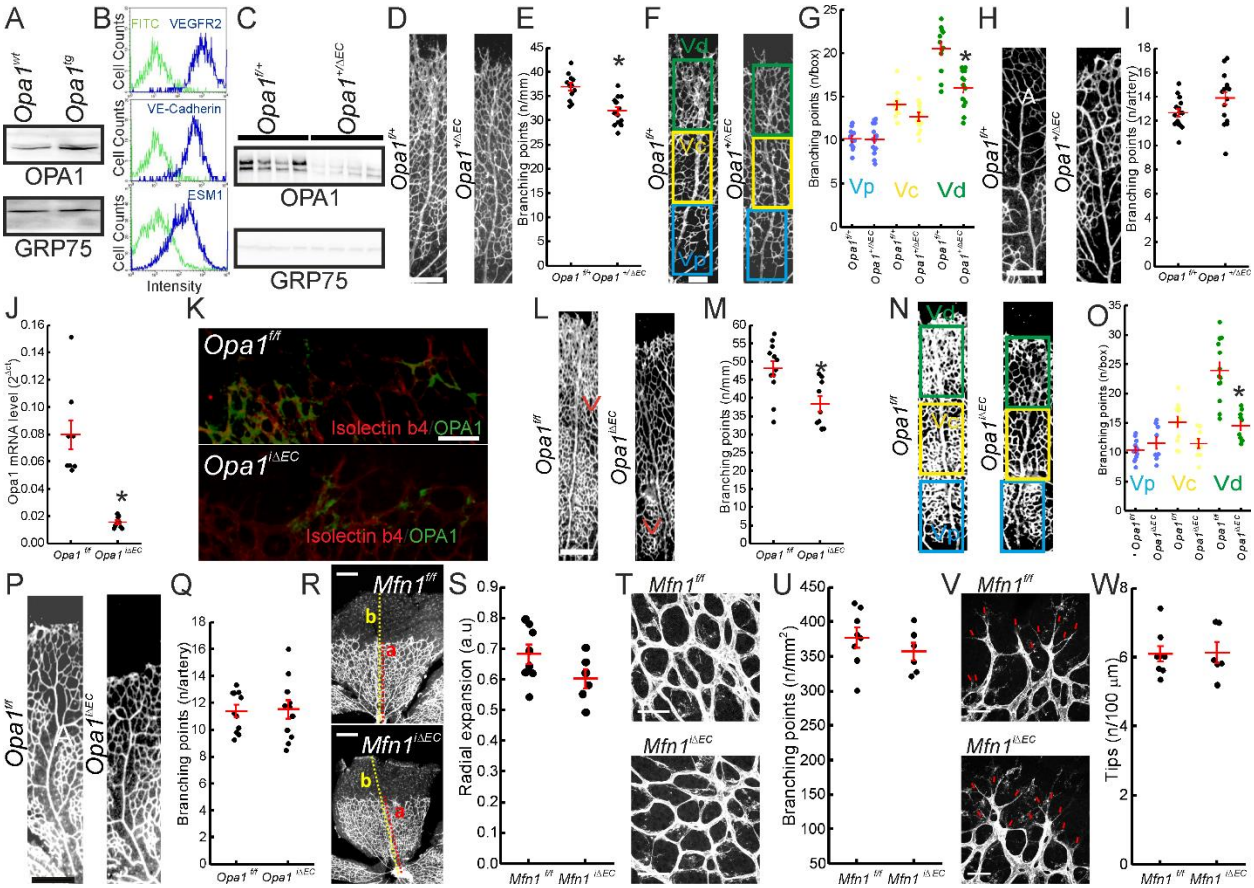

Supplementary Figure 2: OPA1 but not MFN1 ablation affects retinal venous vascularization, related to Fig. 3

(A) Equal amounts of protein MPEC isolated from *Opa1^{tg}* mice were separated by SDS-PAGE and immunoblotted with the indicated antibodies.

(B) FACS analysis of cultured MPECs labelled with antibodies for endothelial-specific markers as indicated, followed by Fluorescein isothiocyanate-conjugated secondary antibody. Green line indicates secondary antibody, blue line indicates anti-VE-cadherin, anti-VEGFR2 or anti-ESM1-specific-IgG.

(C) Equal amounts of protein from MPEC isolated from mice of the indicated genotype were separated by SDS-PAGE and immunoblotted with the indicated antibodies.

(D) Representative isolectin b4 immunofluorescence (magnification 5x) of flat-mounted retinas from 6-day-old pups of the indicated genotype showing a vein. Scale bar: 100 µm.

(E) Quantification of total venous branching points/mm of vein. Experiments were performed as in (D). *: p=0.0002, n=12 Opa1$^{f/+}$ and 13 Opa1$^{+/\Delta EC}$ mice.

(F) Representative isolectin b4 immunofluorescence (magnification 5x) of flat-mounted retinas from 6-day-old pups of the indicated genotype. Blue box: proximal vein (Vp); yellow box: central vein (Vc); green box: distal vein (Vd). Scale bar: 250 µm.

(G) Quantification of proximal, central and distal venous branching points. Experiments were performed as in (F). *: p=9x10^{-5} Opa1$^{f/+}$ vs. Opa1$^{+/\Delta EC}$ Vd. n=12 Opa1$^{f/+}$ and 15 Opa1$^{+/\Delta EC}$ mice.

(H) Representative isolectin b4 immunofluorescence (magnification 5x) of flat-mounted retinas from 6-day-old pups of the indicated genotype. Artery is indicated with A. Scale bar: 100 µm.

(I) Quantification of total arterial branching points. Experiments were performed as in (H). n=15 mice/genotype.

(J) $2^{\Delta ct}$ of *Opa1* mRNA levels determined by RT-PCR in MPECs isolated from 5-day-old pups injected with tamoxifen from P1 to P3. *: p=0.0003, n=9 mice per genotype.

(K) Representative confocal images of flat-mounted retinas from 6-day-old pups of the indicated genotype, stained for OPA1 (green) and isolectin b4 (red). Scale bar: 250 µm.

(L) Representative isolectin b4 immunofluorescence (magnification 5x) of flat-mounted retinas from 6-day-old pups of the indicated genotype showing a vein. Scale bar: 100 µm.
(M) Quantification of total venous branching points/mm of vein. Experiments were performed as in (L). *: p=0.004, n=12 *Opa1$^{f/f}$* and 9 *Opa1$^{i\Delta EC}$* mice.
(N) Representative isolectin b4 immunofluorescence (magnification 5x) of flat-mounted retinas from 6-day-old pups of the indicated genotype. Green box: distal vein (Vd), yellow box: central vein (Vc) and blue box: proximal vein (Vp). Scale bar: 100 µm.
(O) Quantification of proximal, central and distal venous branching points. Experiments were performed as in (F) from 6-day-old pups of the indicated genotype. *: p=2x10^{-5} *Opa1$^{f/f}$* vs. *Opa1$^{i\Delta EC}$* Vd. n=13 *Opa1$^{f/f}$* and 10 *Opa1$^{i\Delta EC}$* mice.
(P) Representative isolectin b4 immunofluorescence (magnification 5x) of flat-mounted retinas from 6-day-old pups of the indicated genotype showing an artery. Scale bar: 100 µm.
(Q) Quantification of total arterial branching points. Experiments were performed as in (P). n=11 mice/genotype
(R) Representative isolectin b4 immunofluorescence (magnification 2.5x) of flat-mounted retinas from 6-day-old pups of the indicated genotype. a (red) indicates the vascular front radius and b (yellow) the retinal radius. Scale bar: 50µm.
(S) Quantification of radial expansion calculated by the ratio a/b in experiments as in (R). n=8 *Mfn1$^{f/f}$* and 6 *Mfn1$^{i\Delta EC}$* mice.
(T) Representative isolectin-b4 immunofluorescence (magnification 5x) of flat-mounted retinas from 6-day-old pups of the indicated genotype. Scale bar: 100 µm.
(U) Quantification of branching points/mm^2 of retina in experiments as in T, n=8 *Mfn1$^{f/f}$* and 6 *Mfn1$^{i\Delta EC}$* mice.
(V) Representative isolectin b4 immunofluorescence (magnification 40x) of flat-mounted retinas from 6-day-old pups of the indicated genotype. Red arrows: tips cells. Scale bar: 20 µm.
(W) Quantification of number of tip cells in experiments as in (V). n=8 *Mfn1$^{f/f}$* and 6 *Mfn1$^{i\Delta EC}$* mice.

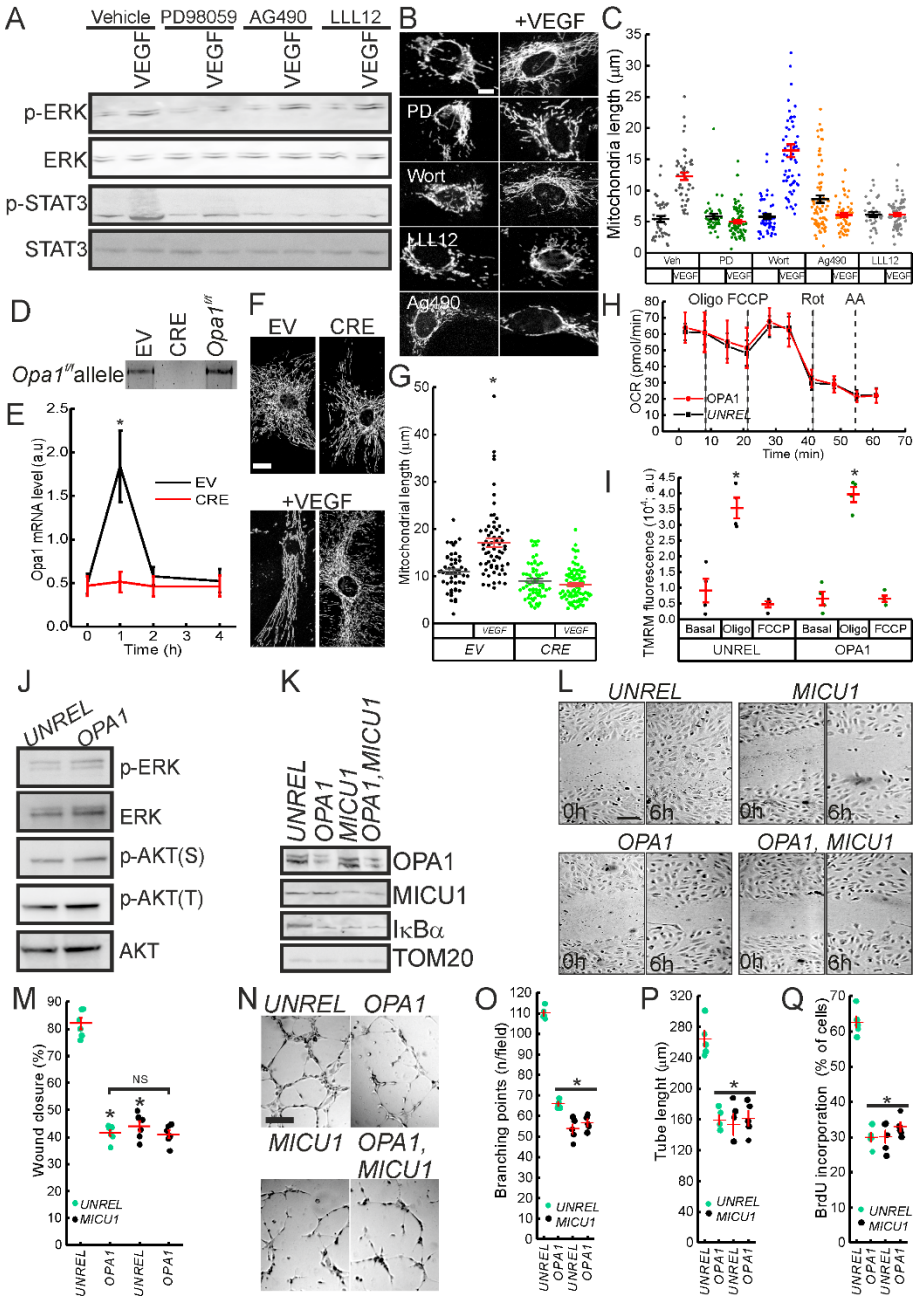

Supplementary Figure 3: OPA1 and MICU1 affect NF□B activation in HUVECs, related to Fig. 4

(A) HUVEC pretreated for 1h where indicated with PD98059, U0126, Wortmaninn or for 3h with LLL12 or AG490 and were treated where indicated with VEGF for 1h. Equal amounts of protein were separated by SDS-PAGE and immunoblotted with the indicated antibodies.

(B) Representative confocal images of mitochondrial morphology in HUVEC treated as indicated and stained for TOM20. Scale bar: 30 μm.

(C) Quantification of mitochondria length in experiments as in B. Each dot represents 1 mitochondrion. *: $p=4x10^{-14}$ vehicle vs. vehicle+VEGF; $p=2X10^{-15}$ wortmannin vs wortmannin+VEGF. n=3 independent experiments.

(D) PCR analysis of genomic DNA from MPEC isolated from *Opa1$^{f/f}$::Opa1^{tg}* mice infected with the indicated adenoviruses.

(E) $2^{\Delta ct}$ of *OPA1*mRNA levels determined by RT-PCR in *Opa1$^{f/f}$::Opa1^{tg}* MPEC infected with the indicated adenovirus and treated for 1 h as indicated.*: $p<0.05$, n=4.
(F) Representative confocal images of mitochondrial morphology in *Opa1$^{f/f}$::Opa1^{tg}* MPEC infected with the indicated adenovirus, treated for 2h as indicated. and stained for TOM20. Scale bar: 30 µm.
(G) Quantification of mitochondria length in experiments as in F. Each dot represents 1 mitochondrion. *: $p=5X10^{-6}$. n=3.
(H) OCR in HUVEC transfected as indicated for 48h. Where indicated, oligomycin (Oligo, 0.1µM), carbonyl cyanide-p-trifluoromethoxyphenylhydrazone (FCCP, 1µM), rotenone (Rot, 0.5µM), and antimycin A (AA, 0.5µM) were injected.
(I) Flow cytometric quantification of TMRM fluorescence in HUVEC transfected for 48h with the indicated siRNA and treated as indicated. n=4.
(J, K) Equal amounts of protein extracted from HUVEC transfected for 48h with the indicated siRNA were separated by SDS-PAGE and immunoblotted with the indicated antibodies.
(L) Representative brightfield images of a scratch-wound assay with HUVEC transfected with the indicated siRNA for 48h. Scale bar: 100µm.
(M) Quantification of cellular migration at 6h in scratch wound assay experiments as in L. *: $p<0.05$, n=6.
(N) Representative brightfield images of endothelial tubular network HUVEC transfected with the indicated siRNA seeded on Matrigel for 6h. Scale bar: 250 µm.
(O, P) Quantification of branching points (O) and tube length (P) in experiments as in N. *: $p<0.05$, n=5.
(Q) Quantification of cellular proliferation determined by BrdU incorporation after 24h in HUVEC transfected for 48h with the indicated siRNA. *: $p<0.05$, n=5.

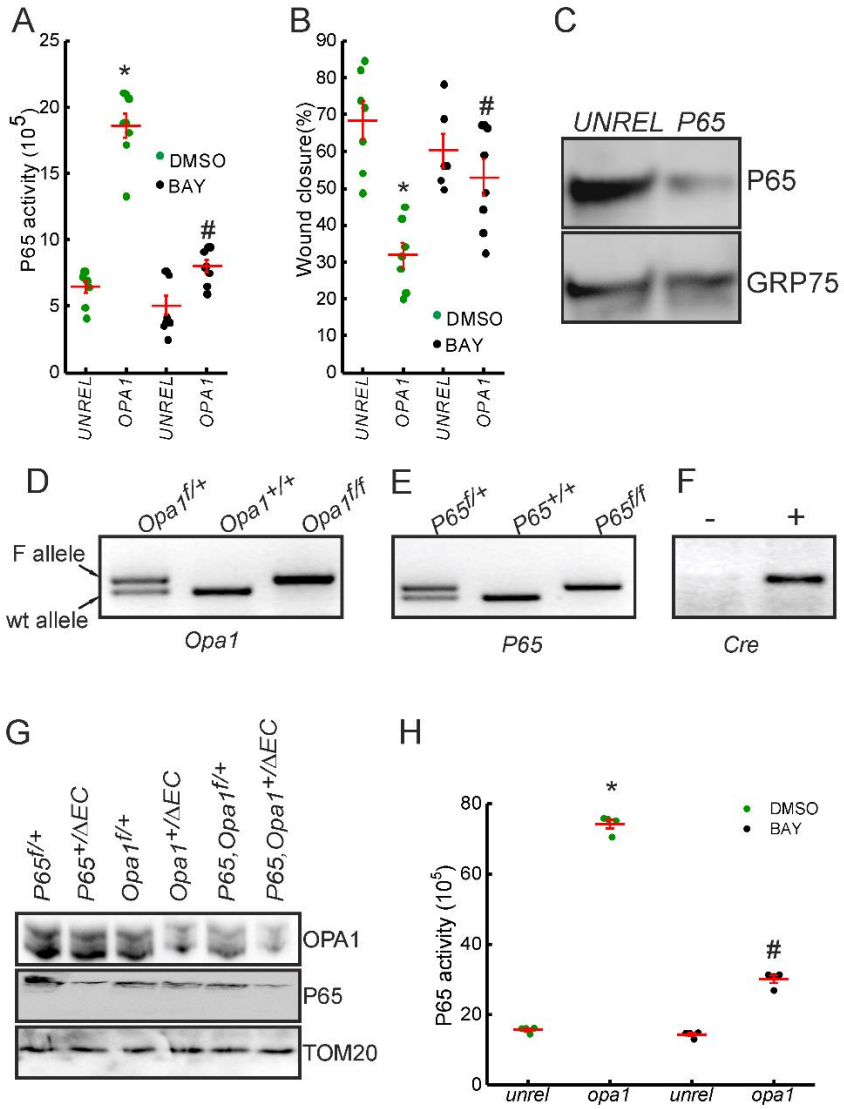

Supplementary Figure 4: *OPA1* ablation impairs angiogenesis by activating the NF□B pathway, related to Fig. 4

(A) P65 DNA-binding ability determined by ELISA on equal amounts of proteins from HUVEC transfected 48h with the indicated siRNA and treated for 6h as indicated. *: p=2x10^{-7} *UNREL*-DMSO vs *OPA1*-DMSO; #: p=8x10^{-7} *OPA1*-DMSO versus *OPA1*-BAY11-7082; n=8.

(B) Quantification of cellular migration determined at 6h in a scratch wound assay of HUVEC transfected for 48h with the indicated siRNA and treated for 6h as indicated. *: p =0.0006 *UNREL*-DMSO vs *OPA1*-DMSO; #: p=0.009 *OPA1*-DMSO vs *OPA1*-BAY11-7082; n=9.

(C) Equal amounts of protein from HUVEC transfected for 48h with the indicated siRNA were separated by SDS-PAGE and immunoblotted with the indicated antibodies.

(D-F) *Opa1* (D), *P65* (E) and *Cre* (F) RT-PCR analysis of transcripts in mice of the indicated genotype.

(G) Equal amounts of protein (20µg) from MPEC isolated from mice of the indicated genotype were separated by SDS-PAGE and immunoblotted with the indicated antibodies.

(H) P65 DNA-binding ability determined by ELISA on equal amounts of protein from Zebrafish injected with *the indicated* morpholinos and treated for 6h as indicated. *: p=4x10^{-6} *unrel*-DMSO vs. *opa1*-DMSO; #: p=2x10^{-7} *opa1*-DMSO vs. *opa1*-BAY11-7082; n=4.

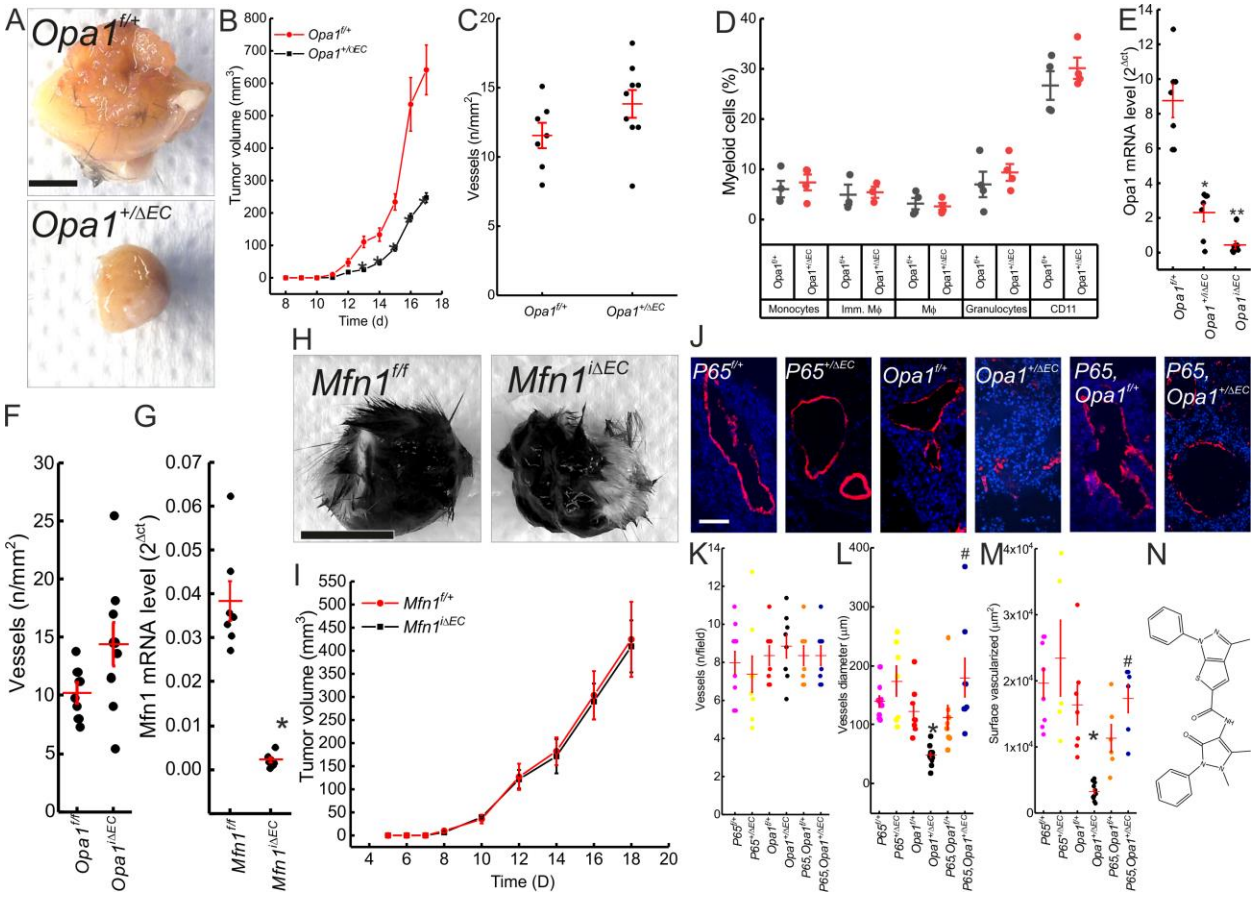

Supplementary Figure 5: Endothelial *Opa1* but not *Mfn1* ablation impairs tumor growth, related to Fig. 5

(A) Photographs of representative breast adenocarcinoma removed after 16 days from subcutaneous implants of $1.5x10^5$ E0771 cells in 6-week-old mice of the indicated genotype. Scale bar: 0.2 cm.

(B) Growth curves of $5x10^4$ B16F10 melanoma cells subcutaneously implanted at day 0 in 6-week-old mice of the indicated genotype. n=7 *Opa1*$^{f/+}$ and 6 *Opa1*$^{+/\Delta EC}$ mice. *: p<0.05.

(C) B16F10 melanomas in experiments as in Figure 5B were removed at day 16, stained with CD31 for blood vessels and number of tumor blood vessels was quantified. n=7 *Opa1*$^{f/+}$ and 9 *Opa1*$^{+/\Delta EC}$ mice.

(D) Percentage of myeloid cells determined by flow cytometry in 500 mm^3 melanomas from $5x10^4$ B16F10 cells implanted subcutaneously in 6-week-old mice of the indicated genotype, n=4 mice/genotype.

(E) $2^{\Delta ct}$ of *OPA1* mRNA levels determined by RT-PCR in MPECs isolated from 6-week-old mice injected with tamoxifen between P15 and P20. *p=0.01 *Opa1*$^{f/+}$ vs *Opa1*$^{+/i\Delta EC}$; **: p=0.0009 *Opa1*$^{f/f}$ vs *Opa1*$^{i\Delta EC}$; n=7 *Opa1*$^{f/f}$ and *Opa1*$^{i\Delta EC/+}$, 6 *Opa1*$^{i\Delta EC}$.

(F) Quantification of number of tumor blood vessels in experiments as in Figure 5F-G performed on mice of the indicated genotype. n=8 *Opa1*$^{f/f}$ and 9 *Opa1*$^{i\Delta EC}$.

(G) $2^{\Delta ct}$ of *Mfn1* mRNA levels determined by RT-PCR in MPECs isolated from 6-week-old mice injected with tamoxifen between P15 and P30. *: $p=1x10^{-5}$, n=7 mice/genotype.

(H) Photographs of representative melanomas removed after 16 days from subcutaneous implants of $5x10^4$ B16F10 cells in 6-week-old mice of the indicated genotype. Scale bar: 0.5 cm

(I) Growth curves of subcutaneously implanted $5x10^4$ B16F10 melanomas at day 0 in 6-week-old mice of the indicated genotype. n=7 mice/genotype.

(J) Representative confocal images of B16F10 melanomas in experiments as in Figure 5K-L stained with Hoechst (blue) and CD31 (red) to label blood vessels. Scale bar: 200 µm.

(K-M) Quantification of number of tumor vessels number (K), diameter (L) and surface (M) in experiments as in J. *: p=1x10^{-5} *Opa1$^{fl/+}$ vs. Opa1$^{+/\Delta EC}$*: #: p=0.05 *Opa1$^{+/\Delta EC}$ vs P65,Opa1$^{+/\Delta EC}$* in (L). *: p =0.002 *Opa1$^{fl/+}$ vs. Opa1$^{+/\Delta EC}$*; #: p=0.007 *Opa1$^{+/\Delta EC}$ vs. P65,Opa1$^{+/\Delta EC}$* in (M). n=7 mice/genotype.
(N) Chemical formula of the Opa1 inhibitor N-(1,5-dimethyl-3-oxo-2-phenyl-2,3-dihydro-1H-pyrazol-4-YL)-3-methyl-1-PH+ (MYLS22).

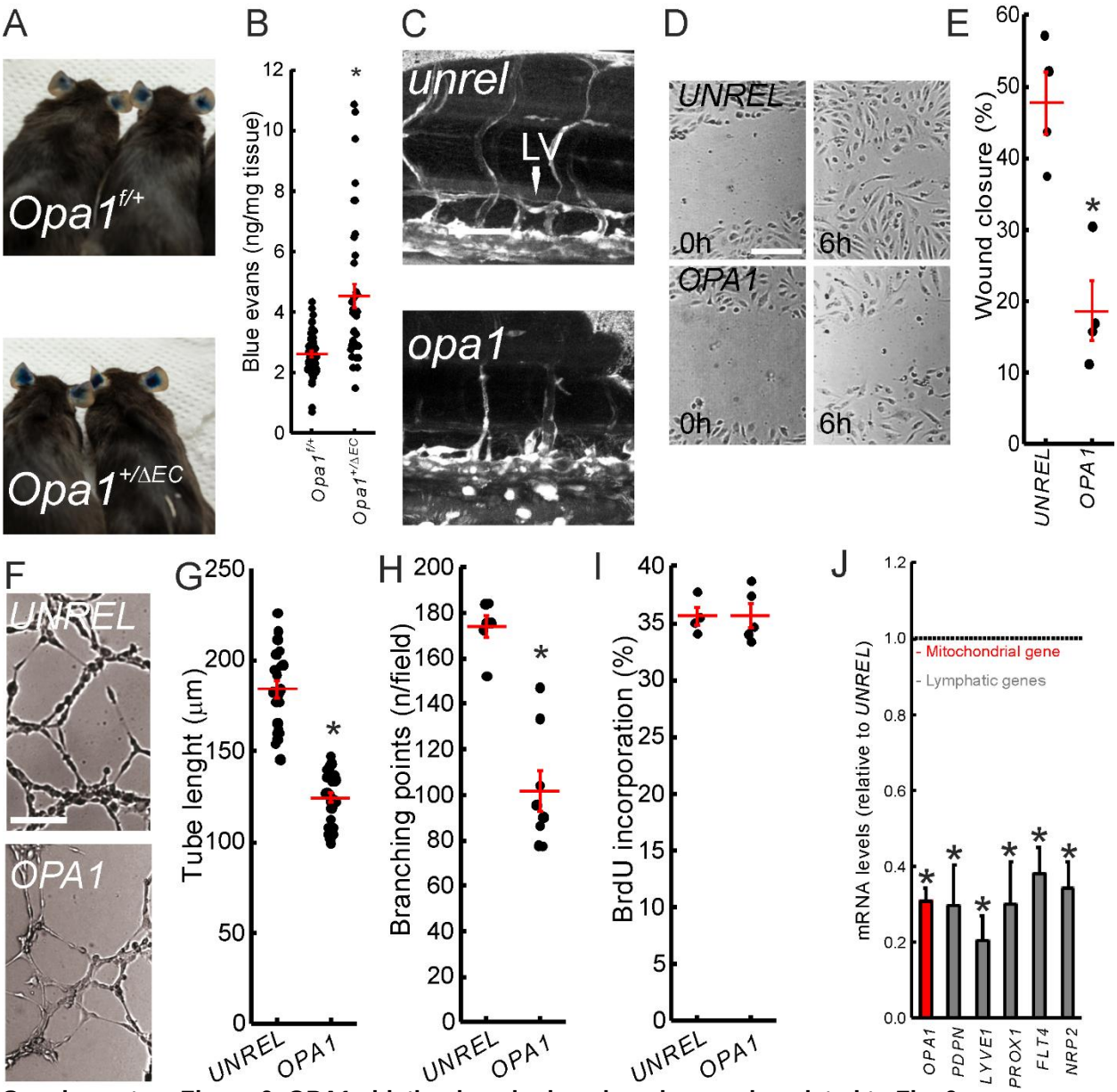

Supplementary Figure 6: OPA1 ablation impairs lymphangiogenesis, related to Fig. 6

(A) Representative pictures of 6-week-old mice of the indicated genotype mice 16h after Evan's blue intradermal ear injection.

(B) Quantification of Evan's blue dye in ear skin in experiments were performed as in (A). *: $p=2x10^{-5}$, n=50 *Opa1*$^{f/+}$ and 37 *Opa1*$^{+/\Delta EC}$ mice.

(C) Representative confocal images of trunk venous and lymphatic vessels of Zebrafish Tg (*stab1:YFP*) 5 days after the injection of the indicated morpholino. LV: lymphatic vessels. Scale bar: 150 µm.

(D) Representative brightfield images of a scratch-wound assay of HMVEC-dly transfected for 48h with the indicated siRNA. Scale bar: 100 µm.

(E) Quantification of cellular migration at6 h in experiments as in (D). *: p=0.003, n=4

(F) Representative brightfield images of the lymphatic tubular network of HMVEC-dly transfected for 48h with the indicated siRNA and seeded on Matrigel for 6h. Scale bar: 250 µm.

(G) Quantification of tube length in experiments as in (F). *: $p=4x10^{-13}$, n=25.

(H) Quantification of branching points in experiments as in (F). *: $p=3x10^{-5}$, n=6.

(I) Quantification of cellular proliferation determined by measuring BrdU incorporation after 24h in HMVEC-dly transfected for 48h with the indicated siRNA. n=4.
(J) Average±SEM of 4 independent RT-PCR analyses of the indicated genes in HMVEC-dly transfected 32h with *OPA1* siRNA, normalized to a non-related human sequence (*UNREL*) siRNA. *: $p<0.05$.

Supplementary Tables

Primers for human genes (qPCR)	Sequence 5'-3'
hs *PODOPLANIN* for	GTGTAACAGGCATTCGCATCG
hs *PODOPLANIN* rev	TGTGGCGCTTGGACTTTGT
hs *PROX1* for	AAAGTCAAATGTACTCCGCAAGC
hs *PROX1* rev	CTGGGAAATTATGGTTGCTCCT
hs *LYVE1* for	AATTTCACAGAAGCTAAGGAGGC
hs *LYVE1* rev	TCAAGGCTGTTTCAACTTGGTC
hs *NRP2* for	CCCTCACTTTGAAATCGAGAAGC
hs *NRP2* rev	CTGCGGATTCACTGTCCCC
hs*VEGFR3* for	TGCAAGAGGAAGAGGAGGTCT
hs*VEGFR3* rev	CAGGCTTGGCGGGCTGTCC
hs *OPA1* for	CGACCCCAATTAAGGACATCC
hs *OPA1*rev	GCGAGGCTGGTAGCCATATTT
hs *DRP1* for	CACCCGGAGACCTCTCATTC
hs *DRP1* rev	CCCCATTCTTCTGCTTCCAC
hs *MFN1* for	ATGACCTGGTGTTAGTAGACAGT
hs *MFN1* rev	AGACATCAGCATCTAGGCAAAAC
hs *MFN2* for	CACATGGAGCGTTGTACCAG
hs *MFN2* rev	TTGAGCACCTCCTTAGCAGAC
hs *VEGFa* for	CTCTACCTCCACCATGCCAAGT
hs *VEGFa* rev	TGCGCTGATAGACATCCATGA
hs *SERPIN* for	CATGCCCTTGTCATCAATCTTG
hs *SERPIN* rev	CATGCCCTTGTCATCAATCTTG
hs *PDGFb* for	AACAACCGCAACGTGCAGT
hs *PDGFb* rev	GTCACCGTGGCCTTCTTAAAGA
hs *EPHRINb2* for	CGTGCTGGAGAATTGACTGA
hs *EHRINb2* rev	CTGTCTTCCCTTGGCTTCTG
hs *EPHRIN b4* rev	TTGATTGCCACACAGCTCTC
hs *EPHRIN b4* for	GGTCTACATCGACCCCTTCA
hs *CDH5* for	ATGAGAATGACAATGCCCCG
hs *CDH5* rev	TGTCTATTGCGGAGATCTGCAG
hs *FGFR* for	ATAAAAAGACAACCAACGGCCG
hs *FGFR* rev	ACCCCGAAAGACCACACATCA
hs *PPIA* for	CCAACACAAATGGTTCCCAGT
hs *PPIA* rev	CCATGGCCTCCACAATATTCA
hs *β-2MiCROGLOBULIN*rev	AATCCAAATGCGGCATCT
hs *β 2MiCROGLOBULIN* for	GAGTATGCCTGCCGTGTG

Table S1: List of oligonucleotides used for human QRT-PCR (related to key resources table)

Primers for murine genes (qPCR)	Sequence 5'-3'
mm *opa1*for	ATACTGGGATCTGCTGTTGG
mm *opa1* rev	AAGTCAGGCACAATCCACTT
Mm *actin* for	ACGGCCAGGTCATCACTATTG
Mm *actin* rev	AGGAAGGCTGGAAAAGAGCC

Table S2: List of oligonucleotides used for mouse QRT-PCR (related to key resources table)

Allele	Sequences 5'-3'
mito ec gfp for	TCTTCTTCAAGGACGACGGCAACT
mito ec gfp rev	CCTTGATGCCGTTCTTCTGCTTGT
Opa1$^{f/f}$ for	CAGTGTTGATGACAGCTCAG
Opa1$^{f/f}$ rev	CATCACACACTAGCTTACATTTGC
cre for	GCGGTCTGGCAGTAAAAACTATC
cre rev	GTGAAACAGCATTGCTGTCACTT
P65$^{f/f}$ for	GAGCGCATGCCTAGCACCAG
P65$^{f/f}$ rev	GTGCACTGCATGCGTGCAG

Table S3: List of oligonucleotides used for mouse genotyping (related to key resources table)

Supplementary datasets

Dataset 1. Pathways modified in HUVEC treated with VEGF for 1, 4 and 12h.

The list was generated from the transcriptional changed genes from ANGIOGENES database of RNA sequencing analyzed by SPIA.

Dataset 2. Differentially expressed genes upon Opa1 silencing in HUVEC

The list was obtained from triplicates analyses of control and Opa1-ablated HUVECs (fold change threshold=0.6 FDR=0.05). Raw sequenced reads were aligned by using STAR (reference genome HOMO SAPIENS UCSChg19). Fold change was calculated using *DESeq2* (*v*. *1.6.3*).

Supplemental dataset 1

Click here to access/download

Supplemental Videos and Spreadsheets

supplementary dataset 1.xlsx

Supplemental dataset 2

Click here to access/download

Supplemental Videos and Spreadsheets

supplementary dataset 2.xlsx